

TAILORING THE GEOMETRY OF MICRON SCALE RESONATORS TO
OVERCOME VISCOUS DAMPING
MARGARITA VILLA

Thesis submitted to the Faculty of the
Virginia Polytechnic Institute and State University
in Partial Fulfillment of the Requirements for the Degree of
MASTER OF SCIENCE

in
Mechanical Engineering

Mark R. Paul, Chair

Daniel J. Inman

Bahareh Behkam

May 1, 2009

Blacksburg, Virginia

Keywords: doubly-clamped beams, quality factor, microfluidics, Brownian motion, viscous dissipation

Abstract

TAILORING THE GEOMETRY OF MICRON SCALE RESONATORS TO
OVERCOME VISCOUS DAMPING
MARGARITA VILLA

Improving the quality factor of the mechanical oscillations of micron scale beams in a viscous fluid, such as water, is an open challenge of direct relevance to the development of future technologies. We study the stochastic dynamics of doubly-clamped micron scale beams in a viscous fluid driven by Brownian motion. We use a thermodynamic approach to compute the equilibrium fluctuations in beam displacement that requires only deterministic calculations. From calculations of the autocorrelations and noise spectra we quantify the beam dynamics by the quality factor and resonant frequency of the fundamental flexural mode over a range of experimentally accessible geometries. We carefully study the effects of the grid resolution, domain size, linear response, and time-step for the numerical simulations. We consider beams with uniform rectangular cross-section and explore the increased quality factor and resonant frequency as a baseline geometry is varied by increasing the width, increasing the thickness, and decreasing the length. The quality factor is nearly doubled by tripling either the width or the height of the beam. Much larger improvements are found by decreasing the beam length, however this is limited by the appearance of additional modes of dissipation. Overall, the stochastic dynamics of the wider and thicker beams are well predicted by a two-dimensional approximate theory beyond what may be expected based upon the underlying assumptions, whereas the shorter beams require a more detailed analysis.

Acknowledgments

I would like to thank my advisor for inspiring and guiding me throughout my graduate studies. Most importantly, I thank my mom, brother, boyfriend and family for their support and encouragement to continue my graduate studies at Virginia Tech. Finally, I want to acknowledge laboratory mates and friends for their contribution and help.

Table of Contents

Abstract	ii
Acknowledgments	iii
Table of Contents	iv
List of Tables	vi
List of Figures	ix
Nomenclature	xvi
1 Introduction	1
1.1 Modes of Actuation	4
1.2 The Challenge of High Quality Oscillations in Fluid	6
2 The Dynamics of Doubly-Clamped Beams	8
3 Quantifying the Dynamics of Doubly-Clamped Beams in a Viscous Fluid	11
3.1 Analytical Prediction	11
4 Numerical Approach	16
4.1 Autocorrelation of Equilibrium Fluctuations in Displacement . .	16
4.2 Three-Dimensional Computations	18
4.3 Validation of Theory with Numerics	18
4.4 Validation of the Numerics	20
4.4.1 Grid Study	21
4.4.2 Size of the Numerical Domain	22

4.4.3	Negligible Convective Inertia	24
4.4.4	Time-Step Study	25
5	Tailoring the Geometry of Doubly-Clamped Beam	33
5.1	Beam Geometry Study	33
6	Flow Field Analysis	42
6.1	Axial Flow Field	42
7	Conclusions	48
	List of References	49

List of Tables

1	The baseline geometry of a doubly-clamped beam used in the numerical simulations, case (1). The beam aspect ratios are L/w , L/h , and w/h . The beam is composed of silicon with Young's modulus $E = 210$ GPa, density $\rho_b = 3100$ kg/m ³ and the fluid is water with $\rho_f = 997$ kg/m ³ , $\mu = 8.56 \times 10^{-4}$ kg/ms. All simulations are performed at room temperature with $T = 300$ K.	8
2	Comparison of the resonant frequency in vacuum ω_0 and the spring constant k using Euler-Bernoulli beam theory (ω_0 , k) and finite element numerical simulations (ω'_0 , k'). Analytical results are found using Eqs. (19) and (18). Also shown are the ratios ω'_0/ω_0 and k'/k .	22
3	Grid resolution of the eight doubly-clamped beams used in the simulations. N_x is the number of cells in the x -direction. N_y is the number of cells in the y -direction. N_z is the number of elements in the z -direction. The three-dimensional fluid simulations have a total number of elements in the beam and a total number of elements in the fluid. The addition of the beam and fluid elements yield the total number of elements of the simulation given in the final column.	24
4	The magnitude of the Stokes boundary layer δ_s and the size of the numerical domain with respect to δ_s . Number of Stokes layers variations with respect to the geometry cases are studied: L_x/δ_s is the number of Stokes layers in the x -direction, L_y/δ_s is the number of Stokes layers in the y -direction and L_z/δ_s is the number of Stokes layers in the z -direction.	25

List of Figures

- | | | |
|---|--|---|
| 1 | A schematic of the fluid flow around a cross-section of a doubly-clamped beam of length L , width w , and thickness h . The flexural oscillations are in the z -direction and the dashed line represents the Stokes layer of thickness δ_s . The schematic also shows the regions of potential and viscous flow around the vibrating beam [39]. | 2 |
| 2 | Scanning electron micrograph of a doubly-clamped beam used in recent experiments demonstrating thermoelastic actuation in vacuum and air [7]. | 5 |
| 3 | (a) A schematic of a cantilever beam with length L , width w , and height h with uniform rectangular cross-section. (b) A doubly-clamped beam used in the numerical simulations with length L , width w , and height h with uniform rectangular cross-section. | 7 |
| 4 | A schematic of a doubly-clamped beam with length L , width w and height h with uniform rectangular cross-section. The beam geometry parameters are given in Table 1. (a) The $x-z$ plane of the beam. (b) The $y-z$ plane of the beam illustrating the rectangular cross-section. In our simulations the beam is immersed in room temperature water and we compute the stochastic dynamics of the fundamental flexural mode driven by Brownian motion. | 8 |

7	The autocorrelations and noise spectra of equilibrium fluctuations in beam displacement. (a) The autocorrelation, normalized using $k/(k_B T)$. (b) The noise spectra, normalized by the peak value, $G(\omega_f)$.	17
8	The deterministic response and power spectrum of the doubly-clamped beam in vacuum. (a) The deterministic response of the beam due to an applied step force. (b) The power spectrum, a dashed line indicates the frequency that maximizes the power spectrum to yield ω_0 .	20
9	The deterministic ring-down of the beam in fluid due to the application of a step force. Z_f is the steady state displacement of the beam. Z_{max} is the maximum displacement of the beam.	21
10	A three-dimensional numerical domain of a doubly-champed beam with 10 elements in the y -direction, 30 elements in the x -direction and 2 elements in the z -direction.	23
11	Grid resolution for cases (1-6). The schematic shows a single quadrant of the fluid and the beam domain. The doubly-clamped beam is located at the center of the volume. The volumes around the beam are composed of fluid. The external surfaces represent the walls bounding the fluid domain. The dashed lines are symmetry boundaries. (a) The $x - z$ plane grid resolution, symmetrically about x and z . (b) The $y - z$ plane grid resolution, symmetrically about y and z .	28

12	Grid resolution for cases (7-8). The schematic includes the fluid and beam. The schematic shows a single quadrant of the fluid and the beam domain. The doubly-clamped beam is located at the center of the volume fixed by two supports. The volumes around the beam are composed of fluid. The external surfaces represent the walls bounding the fluid domain. The dashed lines are symmetry boundaries. (a) The $x - z$ plane grid resolution, symmetrically about x and z . (b) The $y - z$ plane grid resolution, symmetrically about y and z	29
13	Normalized magnitude of the velocity between the beam and the wall in the z -direction. The velocity magnitude $ U $ has been normalized by the maximum velocity $ U_{max} $. The distance between the beam and the wall in the z -direction is normalized by the Stokes length δ_s	30
14	A schematic of the fluid flow regions around a doubly-clamped beam in the $z - y$ plane. The figure is not drawn to scale. The outer box represents a no-slip wall. The beam surface is $15\delta_s$ from the wall.	30
15	A schematic of the domain around a doubly-clamped beam of length L , width w , and height h with a uniform cross section. Shown are the wall-beam distance separations L_x , L_y , L_z in the x , y and z -directions respectively. (a) Numerical domain in the $z - x$ plane. For cases 7 and 8, L_x represents the length of supports. (b) Numerical domain in the $z - y$ plane.	31
16	Quality factor as a function of the number of time steps. The geometry used is case (5) in Table 7. The solid line is a power fit to the data.	32

17	The error E_t as a function of time resolution. The geometry is case (5) in Table 7. The solid line is a power fit to the data and yields $E_t \sim \Delta t^{1.86}$	32
18	The autocorrelations and noise spectra of equilibrium fluctuations in beam displacement as a function of beam width from numerical results: case 1 (w'), case 2 ($2w'$), case 3 ($3w'$). (a) The autocorrelations, the results have been normalized using $k/(k_B T)$ for each case. (b) The noise spectra, the results have been normalized by the peak value for each case, $G(\omega_f)$	37
19	(color) Comparison of numerical results with analytical predictions for Q and ω_f as a function of width w and height h . The circles (blue) are for increasing width and the squares (red) are for increasing height. The solid line is the analytical prediction for increasing width and the dashed line is the analytical prediction for increasing height. To place all values on a single plot $\xi = w/w'$ for the varying width results and $\xi = h/h'$ for the varying height results.	38
20	The autocorrelations and noise spectra as a function of beam height from numerical results: case 1 (h'), case 4 ($2h'$), case 5 ($3h'$). (a) The normalized autocorrelations. (b) The normalized noise spectra.	39
21	The autocorrelations and noise spectra as a function of beam length from numerical results: case 1 (L'), case 6 ($L'/3$), case 7 ($L'/5$), case 8 ($L'/37.5$). (a) The normalized autocorrelations. (b) The normalized noise spectra.	40

22	The variation of the quality Q , panel (a), and of the resonant frequency in fluid ω_f/ω_0 , panel (b), by decreasing the length L of the beam relative to the value of case (1) given by L' . The triangles are the results from numerical simulation and the solid line is the analytical prediction.	40
23	The transverse fluid velocity u_z for cases 1-8 along the line beginning at $(0.0,0.0,0.01\mu\text{m})$ and ending at $(L,0.0,0.01\mu\text{m})$ from the deterministic numerical simulations where the beam velocity is at its maximum value. The baseline geometry is shown as the dashed line, cases 2-7 are the solid lines, and case 8 is the dash-dot line.	41
24	Flow field velocity vectors around a doubly-clamped beam for case 1 at the instant of time where the beam is at its maximum velocity. (a) Flow field over the beam in the the $y - z$ plane. (b) Flow field around the beam in the $x - z$ plane. The dashed vertical line represents symmetry the boundary at $x = L/2$	45
25	Flow field velocity vectors around the doubly-clamped beam for case 7 at the instant of time where the beam is at its maximum velocity. (a) Flow field over the beam in the the $y - z$ plane. (b) Flow field around the beam in the $x - z$ plane. The dashed vertical line represents the symmetry boundary at $x = L/2$	46

26 The normalized axial velocity from numerical simulation. (a)
The axial velocity found varying the width and height of the
baseline geometry. (b) The axial velocity found when decreasing
the length of the baseline geometry. The results for the baseline
geometry are given by the dashed line. The axial velocities are
computed along a line in the x -direction with origin $(0,0,0.01\mu\text{m})$
and end-point $(L,0,0.01\mu\text{m})$, see Fig. 6 for definitions of coordi-
nate directions. The velocity is normalized by u_0 for each case
where u_0 is the maximum transverse velocity which occurs at
 $x = L/2$. The abscissa is normalized by the length L for each case. 47

Nomenclature

$\hat{\cdot}$	Denotes a parameter in the frequency domain, i.e. $\hat{f}(\omega)$
$'$	Denotes values obtained using finite element simulations (unless otherwise noted), i.e. Q'
$\langle \rangle$	Equilibrium ensemble average
R_0	Frequency parameter at resonant frequency in vacuum
R_f	Frequency parameter at the resonant frequency in fluid
R_u	Reynolds Number
T_0	Mass loading parameter
δ_s	Stokes length, (m)
E	Young's modulus, (N/m^2)
η	Mass per unit length, (kg/m)
η_E	Error, (%)
f_0	Resonant frequency in vacuum, (Hz)
F_0	Force magnitude, (N)
$G(\omega)$	Noise spectrum (m^2/Hz)
$\gamma_f(\omega)$	Fluid damping, (kg/s)
$\Gamma(\omega)$	Hydrodynamic function
$\Gamma_i(\omega)$	Imaginary part of the hydrodynamic function
$\Gamma_r(\omega)$	Real part of the hydrodynamic function
I	Moment of inertia, (m^4)
k	Spring constant, (N/m)
k_B	Boltzmann's constant ($1.38 \times 10^{-23} \text{ J/K}$)
Kn	Knudsen number
K_1, K_0	Bessel fuctions
w	Beam width, (m)
h	Beam thickness, (m)
L	Beam length, (m)

λ	Average free path between molecular collisions, (m)
m_{cyl}	Mass of a cylinder of fluid, (kg)
m_e	Effective mass, (kg)
m_f	Fluid loaded mass, (kg)
μ	Dynamic viscosity, (kg/m s)
ν_f	Kinematic viscosity, (m ² /s ²)
N_x	Number of finite elements in the x -direction
N_y	Number of finite elements in the y -direction
N_z	Number of finite elements in the z -direction
ω	Frequency, (rad/s)
$\tilde{\omega}$	Reduced frequency
ω_0	Resonant frequency in vacuum, (rad/s)
ω_f	Resonant frequency in fluid, (rad/s)
p	Pressure, (N/m ²)
Q	Quality factor
ρ_b	Solid density, (kg/m ³)
ρ_f	Fluid density, (kg/m ³)
t	Time, (s)
Δt	Time step, (s)
T	Temperature, (K)
\vec{u}	Velocity vector, (m/s)
U	Velocity, (m/s)
U_{max}	Maximum velocity, (m/s)
u_x	Axial velocity, (m/s)
u_z	Transverse velocity, (m/s)
$z_1(t)$	Stochastic beam displacements, (m)
$\langle x^2 \rangle$	Mean-squared displacement, (m ²)
Z_f	Steady state displacement of $Z_1(t)$, (m)

$Z_1(t)$	Deterministic deflections, (m)
$\langle z_1(t), z_1(t) \rangle$	Autocorrelation of equilibrium fluctuations, (m^2)
γ_f	Viscous damping, (N s/m)
α	Correction factor for equivalent mass
f	Frequency, (Hz)
P_v	Period of oscillation in vacuum, (s)
P_f	Period of oscillation in fluid, (s)
N_v	Number of time steps per oscillation in vacuum
N_f	Number of time steps per oscillation in fluid
Δt_f	Time step in fluid, (s)
L_x	Wall-beam distance separations in the x -direction, (m)
L_y	Wall-beam distance separations in the y -direction, (m)
L_z	Wall-beam distance separations in the z -direction, (m)

1 Introduction

There is a growing need for fast and sensitive micro and nanoscale sensors and actuators that operate in viscous fluid environments. Cutting edge research involving micro-electromechanical systems (MEMS) has the potential to make a significant impact on the fields of medicine, fluid mechanics, and biology [57]. MEMS offer opportunities for sensitive chemical, biological, and physical measurements [4, 5, 40]. Indeed, MEMS are being actively used for mass detection of single molecules in vacuum [3, 56]. With this in mind, one of our main motivations is the prospective that micron scale technology could bring a remarkably fast, on-chip, and robust sensor for technological applications in a viscous fluid.

Many current micro scale technologies are based upon the dynamics of small elastic beams in viscous fluid because of their performance characteristics and high quality factor observed in vacuum [7, 24, 38, 51]. The quality factor Q is the ratio of energy stored by the potential and kinetic energy of the beam, and fluid, to the energy dissipated per oscillation. Currently, experimentalists are trying to obtain high quality factors, $Q \gtrsim 50$, for small beams oscillating in viscous fluid. However, this is a challenge as the beams become smaller because the quality factor gets significantly lower due to the dominance of viscous damping over inertia. The unsteady fluid boundary layer formed around the oscillating solid adds significantly to the added mass which also reduces the resonant frequency of the beam. The Stokes length δ_s is the thickness of this unsteady viscous boundary layer [46], see Fig. 1. The Stokes length is inversely proportional to the frequency as $\omega^{-1/2}$ and increases dramatically when a beam is placed in a viscous fluid. This large boundary layer thickness is a problem for many of the proposed applications of MEMS devices in viscous fluids.

Indeed, due to the length, force and time scales involved, the dynamics of micro scale beams in fluid is dominated by viscosity, while inertia is insignificant.

This problem has attracted considerable attention [29, 31, 43]. With this in mind, it is important to build a physical understanding of micro and nano scale resonators and to develop appropriate analytical models that predict the resulting dynamics and quality factors of the devices in viscous fluid. With a solid understanding of the system, it is anticipated that one could fabricate efficient structures with high quality factors in fluid. This thesis focuses on the physics and modeling issues related to the dynamics of micro scale resonators in viscous fluid to overcome these challenges.

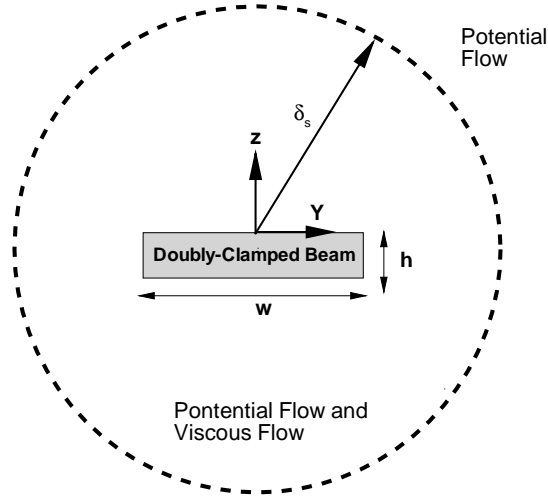


Figure 1: A schematic of the fluid flow around a cross-section of a doubly-clamped beam of length L , width w , and thickness h . The flexural oscillations are in the z -direction and the dashed line represents the Stokes layer of thickness δ_s . The schematic also shows the regions of potential and viscous flow around the vibrating beam [39].

Experimental fabrication and measurements are rapidly approaching the range of $1 \sim 100\text{nm}$ [2]. An understanding of the length, time, and force scales involved is important and it is interesting to compare with relevant biological systems. For a perspective of the length scale: a human hair has a diameter of about $100\mu\text{m}$, a DNA molecule has a diameter of about 2nm , and the diameter

of a single hydrogen atom is about 0.1nm [53]. In this thesis, the nominal dimensions of the studied micron scale beams are between $4\mu\text{m} - 15\mu\text{m}$ for the length, $0.4\mu\text{m} - 5\mu\text{m}$ for the width, and $0.1\mu\text{m} - 0.34\mu\text{m}$ for the thickness.

For a perspective of the force scales of biological systems, the breaking and manipulation of chemical bonds occur at the piconewton scale ($1\text{ pN} = 1 \times 10^{-12}\text{N}$). For example, the force needed to unzip a DNA molecule at room temperature is $9 \sim 20\text{pN}$ [18]. Similarly, the time scales are typically related to chemical reaction rates, protein motion, and protein deformation. For example, protein conformation changes occur on the order of one femtosecond ($1\text{ fs} = 1 \times 10^{-15}\text{s}$) to a few seconds [6]. The nominal period of oscillation of the studied micro scale beams in fluid are $0.1 \sim 0.3\mu\text{s}$. With these biological length, time, and force scales in mind, it is apparent that the dynamics of biological phenomena are comparable to the dynamics of micro scale devices.

Currently, an analytical theory that predicts the dynamics of complex beam geometries of micron scale devices in viscous fluid is not available. However, the dynamics of an infinitely long cylinder oscillating in fluid is well understood [27, 41, 50]. It is possible to use this theory as an approximation of the beam geometries under study here. However, it is not known how accurate this theory is when applied to these micron scale structures of finite size. For this reason, we have performed a computational study and use a time dependent, three-dimensional, finite element method to quantify the beam dynamics [28].

The dynamics of a waving cantilever in fluid is a difficult fluid-solid interaction problem with moving boundaries and complex geometries. We solve this fluid-solid interaction problem using an available pressure based algorithm [55]. We are most interested in the resonant frequency and quality factor of the geometries studied. Our results quantify the range of applicability of the analytical theory and yield the deviations of the theory for the more extreme geometries.

Computations, such as these, are critical for the development of micron scale sensors that operate in viscous fluid environments.

The rapid growth of micron scale science and technology over the past two decades has been largely enabled by advances in fabrication [23]. The basic fabrication approach for MEMS using upon silicon technology involves electron beam lithography and micromachining techniques. These production techniques can be used to make complex shapes and well defined electromechanical structures. The technology is based on planar concepts using a combination of electron beam lithography, silicon micromachining techniques, dry etching processes, and lift-off processes [19]. These processes allow the design of various geometries that form mechanical resonators and by metallisation these can be coupled to electrical circuits. Micron and nanoscale applications are usually multidisciplinary and often include electromagnetic, structural, thermal, and fluid interactions [7, 23, 26].

1.1 Modes of Actuation

There are many methods developed to actuate MEMS devices that vary depending on the intended application. Driving methods can use an external apparatus, thermal bombardment of fluid molecules, or an on-device mechanism. For example, two methods are the thermo-optic drive [51] and magnetomotive drive [54]. The optical drive and detection method uses an amplitude-modulated driving diode laser and a continuous wave detection laser. The amplitude tuning of the driving laser causes the resonant actuation of the beam causing the angle of the detection laser to change [51].

The magnetomotive actuation and detection method uses a static magnetic field to induce an electromagnetic force on a beam. Such a beam creates a conducting loop. Since the beam is inside a static magnetic field, a force can be

induced by applying an alternating current through the beam. Therefore, the frequency of the current determines the frequency of oscillation. In addition, detection of the beam displacement can be obtained by using an electronic operational amplifier [20, 23].

Another externally driven technique is to use the inherent thermal motion of the molecules themselves. This driving technique exploits the Brownian motion [1, 11, 54]. For micron scale beams immersed in fluid, the random motion of the fluid molecules induces stochastic fluctuations in the beam displacement. Extensive studies have been done to quantify the dynamics of beams driven by Brownian motion [12, 13, 14, 33].

An elegant on-device technique is thermoelastic actuation [7]. This technique eliminates the use of an external apparatus and the resulting drive dominates the effects of Brownian motion. Thermoelastic actuation expands and contracts the beam due to heating and cooling the top layer of the beam. Thermoelastic actuation is a robust and compact approach for use with MEMS devices. For example, thermoelastic actuation has been successfully demonstrated for doubly-clamped beams in vacuum and air [21]. In this case, the system was made of silicon nitride with thermoelastic actuation and piezoelectric detection resulting in megahertz (MHz) frequency resolution, see Fig. 2.

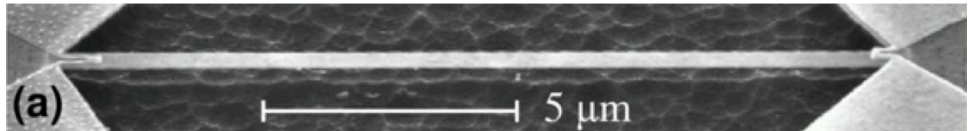


Figure 2: Scanning electron micrograph of a doubly-clamped beam used in recent experiments demonstrating thermoelastic actuation in vacuum and air [7].

Another approach is piezoelectric actuation [34]. A piezoelectric element induces beam displacements by converting an electric field into mechanical strain.

The beam is typically driven at mechanical resonance by varying the applied voltage. A separate piezoelectric element is utilized as a sensor of the beam displacement [2].

1.2 The Challenge of High Quality Oscillations in Fluid

In a fluid environment, the relative magnitude of viscous forces to inertial forces is large resulting in a dramatic reduction in the quality factor and resonant frequency of the fundamental mode of oscillation. For example, the dynamics of a nanoscale cantilever in water can be overdamped [37]. Several approaches have been proposed to overcome this difficulty, including the use of the higher order flexural modes [7, 8, 10, 25, 45], nonlinear feedback control strategies for the external drive [42, 47], and by embedding the fluid inside the cantilever while it oscillates [26, 44].

In this thesis, we have focused on the dynamics of doubly-clamped beams in fluid. These geometries have the potential to form the central component of a robust, compact, and fast detector or actuator. We explored the variation in beam dynamics as a function of its geometry. In particular, we quantified the stochastic dynamics of doubly-clamped beams for a range of sizes and geometries, as well as determined the effectiveness of tailoring the geometry to increase the quality factor and resonant frequency in fluid.

We calculated the stochastic dynamics of the doubly-clamped beams in fluid, see Fig. 3(b), using a thermodynamic approach [36]. The approach requires only a single deterministic calculation of the fluid dissipation that is used to compute the stochastic beam displacement via the fluctuation-dissipation theorem. For a doubly-clamped beam, the deterministic calculation is the ring-down of the beam due to the removal of a step force applied to the center of the beam. We emphasize that the only assumptions in this result are classical dynamics and

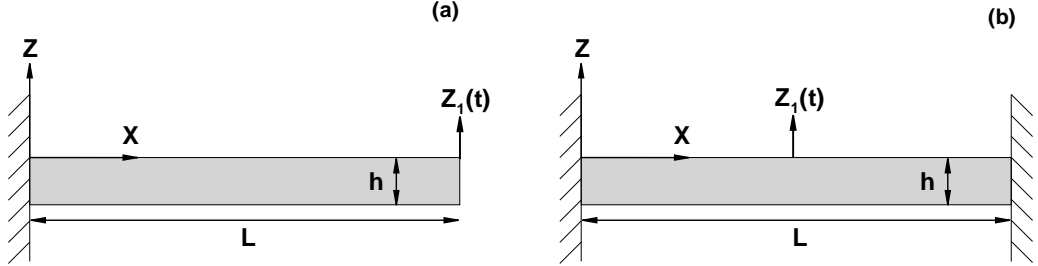


Figure 3: (a) A schematic of a cantilever beam with length L , width w , and height h with uniform rectangular cross-section. (b) A doubly-clamped beam used in the numerical simulations with length L , width w , and height h with uniform rectangular cross-section.

small deflections.

Using three-dimensional, time dependent, finite element simulations for the precise geometries of interest, the stochastic dynamics are computed. In particular, we calculated the autocorrelations, and noise spectra of equilibrium fluctuations in the beam displacement. An analytical approach based on an oscillating infinite cylinder is used to predict the stochastic dynamics and dissipation present. The analytical approach is valid for long slender beams whereas the numerics are valid for any geometry [36, 41].

2 The Dynamics of Doubly-Clamped Beams

In order to build a physical understanding of the stochastic dynamics of microscale doubly-clamped beams in fluid, it is important to first understand the dynamics of the beam in vacuum and to then explore the dynamics of the beam in fluid.

A doubly-clamped beam with a uniform rectangular cross-section is shown in Fig. 4. The beam properties considered as a baseline geometry in this thesis are given in Table 1.

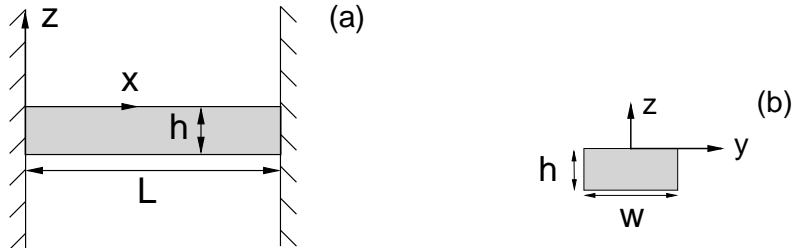


Figure 4: A schematic of a doubly-clamped beam with length L , width w and height h with uniform rectangular cross-section. The beam geometry parameters are given in Table 1. (a) The $x - z$ plane of the beam. (b) The $y - z$ plane of the beam illustrating the rectangular cross-section. In our simulations the beam is immersed in room temperature water and we compute the stochastic dynamics of the fundamental flexural mode driven by Brownian motion.

Case	L [μm]	w [μm]	h [μm]	L/w	L/h	w/h
(1)	15	0.4	0.1	37.5	150	4

Table 1: The baseline geometry of a doubly-clamped beam used in the numerical simulations, case (1). The beam aspect ratios are L/w , L/h , and w/h . The beam is composed of silicon with Young's modulus $E = 210$ GPa, density $\rho_b = 3100$ kg/m³ and the fluid is water with $\rho_f = 997$ kg/m³, $\mu = 8.56 \times 10^{-4}$ kg/ms. All simulations are performed at room temperature with $T = 300$ K.

The beam is modeled using Euler-Bernoulli beam theory [32],

$$EI \frac{\partial^4 Z(x, t)}{\partial x^4} + \eta \frac{\partial^2 Z(x, t)}{\partial t^2} = F(x, t), \quad (1)$$

with boundary conditions

$$Z(0, t) = \frac{\partial Z(0, t)}{\partial x} = 0, \quad (2)$$

$$Z(L, t) = \frac{\partial Z(L, t)}{\partial x} = 0, \quad (3)$$

where the deflection and slope of the beam vanish at the boundaries $x = 0$, $x = L$.

Since the doubly-clamped beam is micron scale, it is important to check whether the continuum mechanics hypothesis is still valid. A useful nondimensional parameter is the Knudsen number,

$$Kn = \frac{\lambda}{L}, \quad (4)$$

where λ is the mean free path between collision for fluid molecules and L is the characteristic length scale. The diameter of a water molecule is $\lambda \approx 0.3\text{nm}$ and the half width of the beam $w/2 = 0.2\mu\text{m}$ is used for the characteristic length L . This yields,

$$Kn = \frac{0.3\text{nm}}{0.2\mu\text{m}} = 1.5 \times 10^{-3}, \quad (5)$$

indicating that the continuum mechanics and the no-slip boundary assumptions are valid [30].

The equations governing the fluid dynamics around the beam are the nondimensionalized Navier-Stokes equations [35] given by

$$R \frac{\partial \vec{u}}{\partial t} + R_u \vec{u} \cdot \vec{\nabla} \vec{u} = -\vec{\nabla} p + \nabla^2 \vec{u}, \quad (6)$$

$$\vec{\nabla} \cdot \vec{u} = 0, \quad (7)$$

where \vec{u} is the fluid velocity, p is the pressure, and t is time. Equations (6)-(7) represent the conservation of momentum and mass for an incompressible fluid. The nondimensional parameters multiplying the two inertial terms are R and R_u . R is the frequency based Reynolds number given by

$$R = \frac{\omega w^2}{4\nu}, \quad (8)$$

where ω is the frequency of oscillation, ν is the kinematic viscosity of the fluid, and w is the width of the beam. R is the ratio of local inertia forces to viscous forces. For the micro scale beams studied in this thesis $R > 1$ which implies the local inertia term $\partial\vec{u}/\partial t$ can not be neglected.

The nondimensional parameter R_u is the typical velocity based Reynolds number given by

$$R_u = \frac{Uw}{2\nu}, \quad (9)$$

where U is the velocity of the fluid. R_u is the ratio of convective inertial forces to viscous forces. For the micro scale beams studied in this thesis $R_u \ll 1$ which implies that the nonlinear convective inertia term $\vec{u} \cdot \vec{\nabla}\vec{u}$ can be neglected. However, it is important to check the validity of these assumptions for the parameters of each simulation. Our numerical simulations include the nonlinear convective inertia term neglected by the analytical expressions.

The flow field around a micron scale doubly-clamped beam in fluid contains both potential and viscous flow contribution [39]. The viscous contribution is within the Stokes layer, see Fig. 1, where

$$\delta_s \approx \frac{w}{2} R^{-1/2}. \quad (10)$$

3 Quantifying the Dynamics of Doubly-Clamped Beams in a Viscous Fluid

In many situations of technological and scientific interest, such as atomic force microscopy [9], the elastic beams are long and thin $L \gg w \gg h$. The fluid-solid interaction problem describing the motion of a waving beam in fluid is very difficult with analytical solutions available only under idealized conditions [17, 41, 49]. As discussed, in the limit of small beam displacements, a two-dimensional approximation for the fluid flow over the beam is often used to determine the force interactions with an Euler-Bernoulli beam. This approach has been very successful in predicting the resulting beam dynamics in a viscous fluid [41]. Furthermore, it has been shown that replacing the rectangular beam cross-section with that of a cylinder of diameter equal to the width w yields small errors on the order of several percent [48]. The flow field generated by an oscillating cylinder is well known as well as the forces acting on the surface of the cylinder [39, 46]. These approximations have led to insightful analytical expressions describing the stochastic dynamics of beams in fluid [37, 41]. However, the validity and accuracy of these expressions remain unclear for the finite beam geometries often used in experiment.

3.1 Analytical Prediction

In the limit of a long and thin beam, small displacements, and using the two-dimensional approximation of an oscillating cylinder for the fluid flow, the noise spectrum of equilibrium fluctuations in displacement of the beam measured at $x = L/2$ for the fundamental mode is given by [37],

$$G(\omega) = \frac{4k_B T}{k} \frac{1}{\omega_0} \frac{T_0 \tilde{\omega} \Gamma_i(R_0 \tilde{\omega})}{[(1 - \tilde{\omega}^2(1 + T_0 \Gamma_r(R_0 \tilde{\omega})))^2 + (\tilde{\omega}^2 T_0 \Gamma_i(R_0 \tilde{\omega}))^2]}, \quad (11)$$

where ω is the frequency of oscillation, $\tilde{\omega} = \omega/\omega_0$ is the reduced frequency, ω_0 is the resonant frequency of the fundamental mode in vacuum, R_0 is the frequency

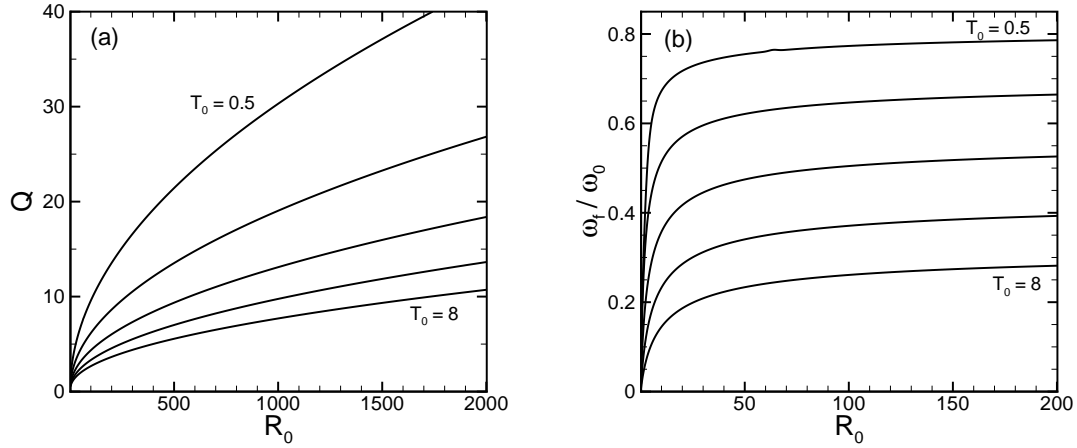


Figure 5: (a) The predicted variation of the quality factor Q for the stochastic displacement of a beam immersed in a viscous fluid with respect to the nondimensional frequency parameter R_0 and mass loading parameter T_0 . (b) The predicted variation of the resonant frequency in fluid ω_f with respect to R_0 and T_0 . In both panels five curves are shown for $T_0 = 0.5, 1, 2, 4, 8$. The bounding two curves are labeled with the remaining curves in sequential order. R_0 is evaluated at the resonant frequency of the beam in vacuum. The quality Q is determined by evaluating Eq. (17) at ω_f where ω_f is the frequency that maximizes Eq. (11).

parameter evaluated at ω_0 , T_0 is the mass loading parameter, k_B is Boltzmann's constant, T is the temperature, and k is the spring constant for the fundamental mode. The frequency parameter evaluated at the resonant frequency in vacuum is,

$$R_0 = \frac{\omega_0 w^2}{4\nu}. \quad (12)$$

In our notation, the frequency parameter R is evaluated at arbitrary frequency ω , and R_f is evaluated at ω_f . The mass loading parameter is

$$T_0 = \frac{\pi \rho_f w}{4 \rho_b h} \quad (13)$$

and represents the ratio of the mass of a cylinder of fluid with radius $w/2$ to the actual mass of the beam where ρ_f is the density of the fluid, and ρ_b is the

density of the beam.

The dynamics of a beam in fluid are not precisely equivalent to that of a damped simple harmonic oscillator. For example, both the mass and damping are frequency dependent. The mass of the entire fluid plus the mass of the beam is

$$m_f(\omega) = m_e(1 + T_0\Gamma_r(R_0\tilde{\omega})) \quad (14)$$

where $m_e = \alpha m_b$ is the equivalent mass of the beam such that the kinetic energy of this mass is equal to that of the fundamental mode and $m_b = \rho_b Lwh$ is the mass of the beam. For the fundamental mode of a doubly-clamped beam $\alpha = 0.396$. The viscous damping is

$$\gamma_f(\omega) = m_{cyl,e}\omega\Gamma_i(R_0\tilde{\omega}) \quad (15)$$

where $m_{cyl,e} = \alpha m_{cyl}$ is the equivalent mass of a cylinder of fluid with diameter equal to w . In the above expressions Γ is the hydrodynamic function for an oscillating cylinder in a viscous fluid [39],

$$\Gamma(\omega) = 1 + \frac{4iK_1(-i\sqrt{iR_0\tilde{\omega}})}{\sqrt{iR_0\tilde{\omega}}K_0(-i\sqrt{iR_0\tilde{\omega}})}, \quad (16)$$

where K_1 and K_0 are Bessel functions, Γ_r and Γ_i are the real and imaginary parts of Γ , respectively and $i = \sqrt{-1}$. As the frequency of oscillation increases the magnitude of m_f decreases and the magnitude of γ_f increases [37].

The simple harmonic oscillator approximation is convenient to define commonly used diagnostics such as the quality factor Q and resonant frequency of the beam in fluid ω_f . As a result of the frequency dependent mass and damping, the fundamental peak of the noise spectra is not well approximated as a Lorentzian for these strongly damped oscillators and care must be taken when determining Q and ω_f . The resonant frequency in fluid ω_f will be defined to be the frequency which maximizes the noise spectrum in Eq. (11). The quality factor Q is then defined as the ratio of energy stored by the potential and

kinetic energy of the beam and fluid to the energy dissipated by viscosity per oscillation when evaluated at ω_f . This yields

$$Q \approx \frac{m_f(\omega_f)\omega_f}{\gamma_f(\omega_f)} = \frac{T_0^{-1} + \Gamma_r(R_0\tilde{\omega}_f)}{\Gamma_i(R_0\tilde{\omega}_f)}. \quad (17)$$

Given values of the nondimensional parameters R_0 and T_0 , Eqs. (11) and (17) directly yield the analytical predictions for ω_f and Q . The variation of Q and ω_f with R_0 and T_0 are shown in Fig. 5 over a large range of parameters. The quality factor increases significantly as the frequency of oscillation is increased and also increases as the mass loading decreases. The drop in the resonant frequency when the beam is placed in fluid, ω_f/ω_0 , also increases with frequency of oscillation and with a reduction in mass loading. The increase of ω_f/ω_0 with respect to R_0 is very rapid for $R_0 \lesssim 20$ with only small changes for higher frequencies, while the dependence upon T_0 results in a nearly uniform increase over the range shown. It is typical for $R_0 \sim 1$ and $T_0 \sim 1$ for many proposed microscale applications in water. In this case the analytics predict strongly damped dynamics with $Q \sim 2$. For applications that require a distinct peak to be measured this presents a significant challenge.

Using Euler-Bernoulli beam theory [32] for a doubly-clamped beam these expressions can be written as a function of geometry (L, w, h) which are often the experimentally relevant parameters rather than R_0 and T_0 . The relevant expressions are,

$$\omega_0 = \frac{11.2}{\sqrt{3}} \sqrt{\frac{E}{\rho_b}} \frac{h}{L^2}, \quad (18)$$

$$k = 16E \left(\frac{h}{L} \right)^3 w, \quad (19)$$

$$R_0 = \frac{2.8}{\sqrt{3}\nu} \sqrt{\frac{E}{\rho_b}} \left(\frac{w}{L} \right)^2 h, \quad (20)$$

where E is the Youngs modulus. These expressions for T_0 and R_0 together with Fig. 5 suggest that Q and ω_f increase by reducing the length, increasing the

width, or increasing the height of the beam. However, the precise improvement is not clear since the available theoretical predictions are only for long and slender beams. In light of this we have performed full time-dependent and three-dimensional finite element numerical simulations [28] of a range of geometries to determine precisely the stochastic dynamics.

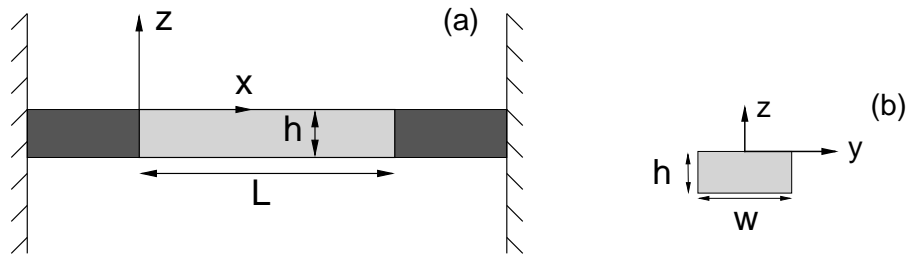


Figure 6: A schematic of a doubly-clamped beam used in the numerical simulations with length L , width w , and height h with uniform rectangular cross-section. (a) The $x - z$ plane of the beam in fluid. The beam is supported by a rigid support of width w on each side. The beam is light grey and the two rigid supports are darker grey. The supports are used to minimize the effects of the bounding side walls for the short-wide geometries. (b) The $y - z$ plane of the beam illustrating the rectangular cross-section. In our simulations the beam is immersed in room temperature water and we compute the stochastic dynamics of the fundamental flexural mode driven by Brownian motion. In the following figures the vertical displacement of the beam at $x = L/2$ is referred to as $z_1(t)$ for thermally induced fluctuations and $Z_1(t)$ for the deterministic ring down simulations.

4 Numerical Approach

This chapter describes the numerical approach used to obtain the stochastic dynamics of the microscale doubly-clamped beams in viscous fluid. This chapter also validates the numerical approach. Three-dimensional computations were used to obtain the complete solution of the fluid-solid structure interactions. To ensure that the numerical simulation parameters did not artificially affect the beam results, a series of validation studies were performed including a grid resolution study, a domain size study, a linear response study, and a time-step study.

4.1 Autocorrelation of Equilibrium Fluctuations in Displacement

We calculated the stochastic dynamics of the doubly-clamped beams in viscous fluid, see Fig. 6, using the thermodynamic approach discussed in detail in Refs. [36, 37]. The autocorrelation of equilibrium fluctuations in beam displacement is calculated from the deterministic ring-down of the beam due to the removal of a step force applied at $x = L/2$ given by

$$F(t) = \begin{cases} F_0 & \text{for } t \leq 0 \\ 0 & \text{for } t > 0 \end{cases} \quad (21)$$

where t is time, and F_0 is the magnitude of the force. The value of F_0 is chosen for each simulation such that the beam deflections remain small and, in this case, the results are independent of its specific value. The autocorrelation of equilibrium fluctuations in beam displacement is then given by,

$$\langle z_1(0)z_1(t) \rangle = k_B T \frac{Z_1(t)}{F_0}. \quad (22)$$

The lower case z_1 indicates stochastic displacement, and upper case Z_1 indicates the deterministic ring-down measured at the center of the beam, $x = L/2$. The noise spectrum of fluctuations in beam displacement is given by,

$$G(\omega) = 4 \int_0^\infty \langle z_1(0)z_1(t) \rangle \cos(\omega t) dt. \quad (23)$$

The noise spectrum is used to determine the resonant frequency in fluid ω_f and the quality factor Q for the numerical results of the doubly-clamped beam. The numerical results for the autocorrelation of equilibrium fluctuations in beam displacement are shown in Fig. 7(a), and the noise spectrum is shown in Fig. 7(b). The resonant frequency ω_f is the frequency maximizing the noise spectrum $G(\omega)$ and the quality is given by

$$Q \approx \frac{m_f(\omega_f)\omega_f}{\gamma_f(\omega_f)} = \frac{k}{4k_B T} \omega_f^2 G(\omega_f). \quad (24)$$

The right hand side of Eq. (24) is found using $m_f(\omega_f) = \sqrt{k/\omega_f}$ and using the peak value of the noise spectrum $G(\omega_f)$ to determine the damping. The error in using the bulk mode spring constant, as opposed to the dynamic spring constant for the fundamental mode, is small and on the order of several percent.

In summary, the numerical procedure is the following:

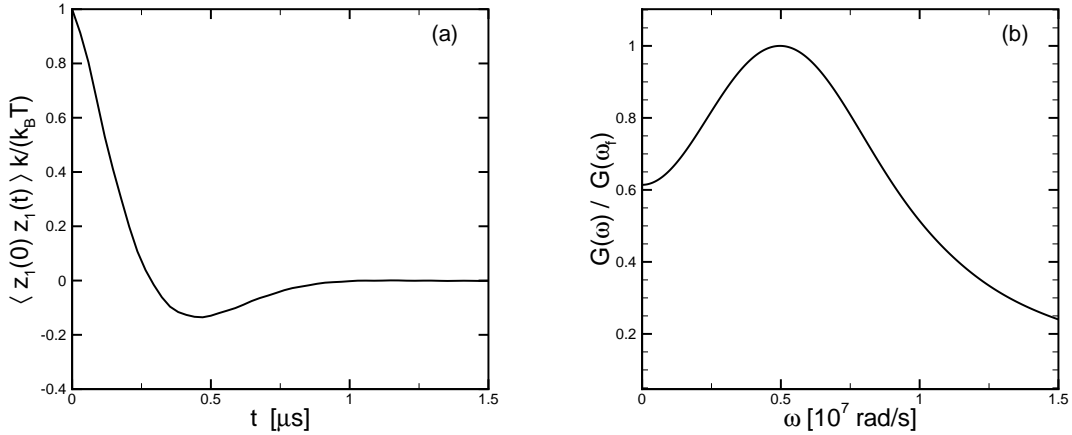


Figure 7: The autocorrelations and noise spectra of equilibrium fluctuations in beam displacement. (a) The autocorrelation, normalized using $k/(k_B T)$. (b) The noise spectra, normalized by the peak value, $G(\omega_f)$.

1. Compute $Z(t)$ from a deterministic simulation of the ring down of the beam due to the removal of a step force.

2. Compute the autocorrelation of equilibrium fluctuations in displacement using Eq. (22).
3. Compute the noise spectrum using Eq. (23).
4. Calculate diagnostics: ω_f is the frequency that maximizes the noise spectrum, and Q is found from Eq. (24).

4.2 Three-Dimensional Computations

We have computed the dynamics of micron scale beams in fluid [28]. We solve the nonlinear, transient, three-dimensional fluid-structure interaction problem using carefully validated numerical simulations.

The three-dimensional computations of the fluid-solid structures use a pressure based algorithm that couples the displacement of the solid structure with the velocity of the fluid structure [55]. This strong pressure-based coupling method consists of solving the incompressible Navier Stokes equations where the fluid structure deformation is induced by a pressure force. The finite volume method was used for evaluating the governing fluid equations at discrete places on the structure that is used to solve the structural dynamics equations. There is not a direct coupling between the solid structure and fluid so these are linked through the grid velocity. The no-slip boundary condition is used so the velocity of the fluid is equal to the velocity of the solid at their interface. This assumption has been shown to be valid at this scale [22].

4.3 Validation of Theory with Numerics

One way to calculate the dynamics of a microscale doubly-clamped beam in vacuum is using Euler-Bernoulli beam theory. The resonant frequency ω_0 and spring constant k are given by Eqs. (18) - (19). The resonant frequency in vacuum from numerics ω'_0 is calculated from the power spectrum. The power

spectrum is the magnitude of the Fourier transform of the beam displacement due to the application of a step-force at $x = L/2$ given by

$$F(t) = \begin{cases} 0 & \text{for } t \leq 0 \\ F_0 & \text{for } t > 0 \end{cases} \quad (25)$$

where t is time, and F_0 is the magnitude of the force. The value of F_0 is chosen such that the beam deflections remain small. We use an upper case Z_1 to indicate the deterministic beam displacement measured at the center of the beam $x = L/2$. The resonant frequency in vacuum ω_0' is the frequency where the peak occurs in the power spectrum. Numerical results for the deterministic response of a doubly-clamped beam are shown in Fig. 8(a), and the power spectrum is shown in Fig. 8(b). In summary, the numerical procedure is the following:

1. Compute $Z_1(t)$: the deterministic response of the beam in vacuum due to an applied step force.
2. Compute the power spectrum, $|\hat{Z}(\omega)|^2$.
3. Calculate ω_0' , the frequency that maximizes the power spectrum.

The spring constant k' of the beam is computed from the deterministic ring-down of the beam in fluid due to a step force applied at $x = L/2$, see Fig. 9. The spring constant could also be calculated using numerical damping. Both approaches are valid, however here the numerical spring constant is determined by performing three-dimensional simulations in fluid. The numerical value of the spring constant is then

$$k' = \frac{F_0}{Z_f}, \quad (26)$$

where Z_f is the steady state displacement due to the step force. The spring constant is computed this way for all of the cases studied in this thesis.

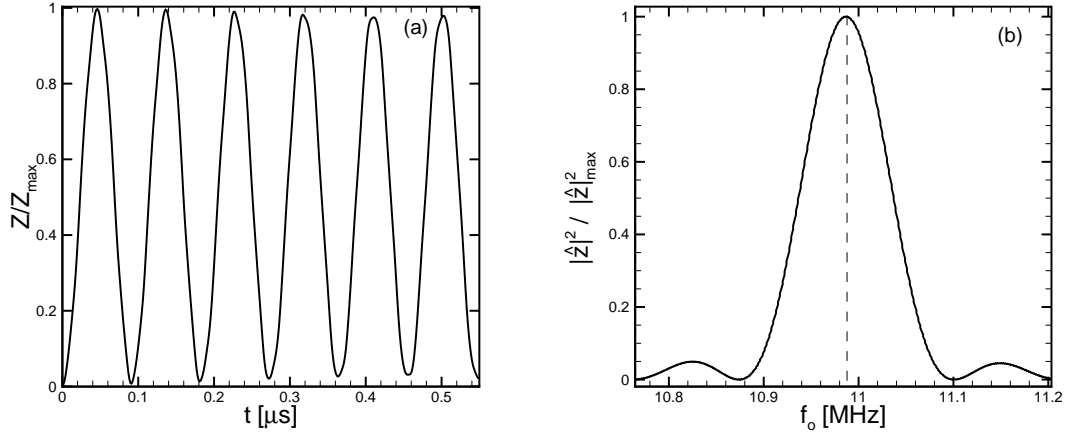


Figure 8: The deterministic response and power spectrum of the doubly-clamped beam in vacuum. (a) The deterministic response of the beam due to an applied step force. (b) The power spectrum, a dashed line indicates the frequency that maximizes the power spectrum to yield ω_0' .

The results show how Euler-Bernoulli theory over predicts ω_0 and k as the length of the beam is reduced, see for example cases (7) and (8). The shorter beams have lower ω_0' and softer k' than an Euler-Bernoulli beam. Values of ω_0 and k are given in Table 4.

In summary, the numerical procedure to calculate the spring constant is:

1. Compute $Z(t)$ from a deterministic ring down of the beam in fluid due to the application of a step force.
2. From the simulation determine the steady state displacement Z_f .
3. Calculate k' using Eq. (26).

4.4 Validation of the Numerics

We quantified the dynamics of a microscale doubly-clamped beam in fluid using finite element numerical simulations. It is important that the computations

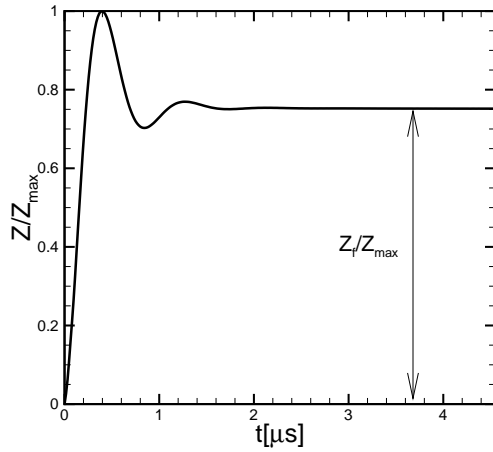


Figure 9: The deterministic ring-down of the beam in fluid due to the application of a step force. Z_f is the steady state displacement of the beam. Z_{max} is the maximum displacement of the beam.

are accurate. We performed a grid resolution study, explored the numerical domain size, ensured linear response, and conducted a time-step study. The validation calculations were performed on a three-dimensional problem.

4.4.1 Grid Study

We performed a grid resolution study of the beam in vacuum with a different number of elements along the beam length, width, and height, see Fig. 10. The variation of elements did not significantly affect the dynamics of the beam in vacuum. However, the numerical domain for beams in fluid can be quite large and the computations are costly. It is preferred to have computationally cost-effective simulations. In order to accomplish this, the grid resolution was decreased adaptively far from the beam surface. In addition, the grid resolution was further customized for the shorter beams, cases (7) and (8). In this case, an additional support was added to reduce any wall effects due to the large average velocity near the wall as shown in Fig. 6. The grid resolutions used are shown

Case	ω'_0 [rad/s]	k' [N/m]	ω_0 [rad/s]	k [N/m]	ω'_0/ω_0	k'/k
(1)	2.31×10^7	0.40	2.36×10^7	0.40	0.978	1.00
(2)	2.44×10^7	0.83	2.36×10^7	0.80	1.034	1.04
(3)	2.43×10^7	1.21	2.36×10^7	1.19	1.029	1.02
(4)	4.65×10^7	3.19	4.72×10^7	3.18	0.984	1.00
(5)	6.84×10^7	10.82	7.09×10^7	10.75	0.965	1.01
(6)	2.19×10^8	10.92	2.13×10^8	10.70	1.028	1.02
(7)	4.97×10^9	1178.95	5.32×10^9	1344	0.935	0.88
(8)	2.46×10^{10}	11413	3.32×10^{10}	21000	0.741	0.54

Table 2: Comparison of the resonant frequency in vacuum ω_0 and the spring constant k using Euler-Bernoulli beam theory (ω_0 , k) and finite element numerical simulations (ω'_0 , k'). Analytical results are found using Eqs. (19) and (18). Also shown are the ratios ω'_0/ω_0 and k'/k .

in Figs. 11 - 12.

The fluid simulations in this thesis have $10^5 \sim 10^6$ elements. The run time varied from $2 \sim 5$ days, depending on the domain size and time step. An average sized fluid simulation has $\sim 5 \times 10^5$ elements and takes approximately three days on a 3.2 GHz Xeon processor with 4GB of DDR memory. When the beam is in fluid, the grid resolution near the beam surface was increased significantly to resolve the fluid dynamics. The grid resolutions used for all of geometries studied are shown in Table 3.

4.4.2 Size of the Numerical Domain

The size of the numerical domain is critical for fluid simulations of microscale doubly-clamped beams. An unnecessarily large domain increases the computational cost. On the other hand, a small numerical domain can introduce undesirable wall effects. Wall effects for microscale devices can damp the beam dynamics, yielding a lower frequency in fluid and a lower quality factor [13, 15, 16]. In order to avoid unwanted wall effects in the numerical simulation, the fluid

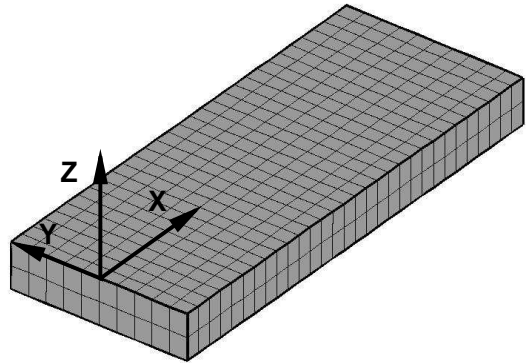


Figure 10: A three-dimensional numerical domain of a doubly-clamped beam with 10 elements in the y -direction, 30 elements in the x -direction and 2 elements in the z -direction.

domain was made large enough to neglect any wall effects. In order to determine this, we computed the magnitude of the velocities near the wall. To ensure the proper size of the fluid domain, the velocities of the fluid should smoothly approach zero at the wall, see Fig 13.

The fluid domain around the microscale doubly-clamped beam has different regions, see Fig 14. Near the surface of the beam, a viscous boundary layer develops (the Stokes layer). Beyond this, the fluid dynamics is dominated by potential flow. To ensure the numerical domain is large enough, we studied a number of domain sizes. A schematic of the domains are shown in Fig 14. Table 4 shows the variation of δ_s for each geometry studied. The numerical results indicate that the distance between the beam and the wall should be $\gtrsim 15\delta_s$.

Beam				Fluid				Total Size	
Case	N_x	N_y	N_z	Total	N_x	N_y	N_z	Total	
(1)	150	4	2	1,200	150	90	68	916,800	918,000
(2)	150	10	2	3,000	150	60	52	465,000	468,000
(3)	30	10	2	600	30	70	62	129,600	130,200
(4)	150	10	2	3,000	150	108	60	969,000	972,000
(5)	72	8	6	3,456	72	64	62	282,240	285,696
(6)	74	10	2	1,480	74	60	62	273,800	275,280
(7)	30	10	2	600	50	62	64	197,800	198,400
(8)	24	24	4	2,304	88	68	60	356,736	359,040

Table 3: Grid resolution of the eight doubly-clamped beams used in the simulations. N_x is the number of cells in the x -direction. N_y is the number of cells in the y -direction. N_z is the number of elements in the z -direction. The three-dimensional fluid simulations have a total number of elements in the beam and a total number of elements in the fluid. The addition of the beam and fluid elements yield the total number of elements of the simulation given in the final column.

4.4.3 Negligible Convective Inertia

In order to ensure the linear response of the system, the Reynolds numbers R_u was evaluated to ensure $R_u \ll 1$. The Reynolds number is based on the ring-down simulation,

$$R_u = \frac{U_{max}w}{2\nu}, \quad (27)$$

where U_{max} is the maximum velocity of the beam. The values of R_0 , R_f and R_u are determined from the numerical simulations. However, it is important to ensure that $R_u \ll 1$ so that the nonlinear convective inertial term can be neglected. This term can become large if the the maximum displacement of the beam is significant $Z_{max} \gtrsim h/10$. The frequency based Reynolds numbers are not negligible if $R_0 \gtrsim 1$ and $R_f \approx 1$. Numerical values of these parameters are given in Table 5.

Case	$\delta_s/(w/2)$	δ_s [μm]	L_x/δ_s	L_y/δ_s	L_z/δ_s
(1)	2.079	0.415	-	14.4	14.4
(2)	0.915	0.366	-	13.7	13.7
(3)	0.586	0.351	-	25	25.4
(4)	0.998	0.199	-	25	15.0
(5)	0.687	0.137	-	31.3	31.6
(6)	0.458	0.091	-	14.2	13.6
(7)	0.078	0.015	64.0	83.3	80.1
(8)	0.033	0.006	193.5	193.5	186.1

Table 4: The magnitude of the Stokes boundary layer δ_s and the size of the numerical domain with respect to δ_s . Number of Stokes layers variations with respect to the geometry cases are studied: L_x/δ_s is the number of Stokes layers in the x -direction, L_y/δ_s is the number of Stokes layers in the y -direction and L_z/δ_s is the number of Stokes layers in the z -direction.

4.4.4 Time-Step Study

We performed a time resolution study of the beam in vacuum for different numbers of time steps per oscillation. The time step for the doubly-clamped beam in vacuum is compared using,

$$f_0 = \frac{\omega_0}{2\pi}, \quad (28)$$

$$P_v = \frac{1}{f}, \quad (29)$$

$$\Delta t = \frac{P_v}{N_v}, \quad (30)$$

where the frequency in vacuum is f_0 , the period of oscillation in vacuum is P_v , the time-step is Δt , and N_v is the number of time steps per period in vacuum. The simulations were run with an increasing number time steps until the variation of the resonant frequency was less than 2%. Approximately 20 steps per oscillation in vacuum was optimal based on computational cost versus accuracy.

One challenge in the numerical simulations is the determination of the appropriate size of the time step for the beam dynamics in fluid. For fluid simulations,

Case	R_0	R_f	R_u	F_0 [nN]
(1)	1.08	0.232	2.71×10^{-2}	3.18
(2)	4.55	1.195	6.82×10^{-3}	0.79
(3)	10.19	2.911	1.14×10^{-3}	0.11
(4)	2.17	1.004	1.45×10^{-3}	0.36
(5)	3.19	2.114	3.05×10^{-3}	1.19
(6)	10.20	4.761	5.58×10^{-2}	10.7
(7)	231.55	164.29	2.4×10^{-4}	0.134
(8)	1146.08	886.81	5.42×10^{-5}	5250

Table 5: The frequency parameters and Reynolds numbers determined from the numerical simulations. The frequency based Reynolds number in vacuum R_0 , the frequency based Reynolds number in fluid R_f and the velocity based Reynolds number in fluid R_u . R_u is evaluated at the maximum deterministic velocity of the beam U_{max} . F_0 is the magnitude of the step force. The values of R_0 , R_f and R_u are determined using the finite numerical simulations.

it is important to have a relationship between the number of time steps in vacuum and the number of time steps in fluid based on the resonant frequency in vacuum ω_0 . When the resonant frequency in fluid ω_f is unknown it is useful to have a time step relationship based on a frequency in vacuum to estimate the time step in fluid. Our results indicate that a fluid simulation could take $19 \sim 98$ time steps per oscillation $P_f/\Delta t$ to accurately resolve the transient motion. The study shows that using 10 to 20 time steps per vacuum oscillation $P_v/\Delta t$ with a well resolved grid resolution and domain size leads to accurate results. Numerical values for the periods of oscillation in fluid and vacuum are shown in Table 6. The table illustrates the time steps, the smallest spatial lengths in the domain, and the total number of elements.

The variation of the quality factor Q with decreasing the time step is also investigated. It is important to determine the time step resolution required to accurately compute the deterministic response of a doubly-clamped beam. We performed a time step study of the doubly-clamped beam (case 5) in fluid

Case	Total Elements	$P_v/\Delta t$	$P_f/\Delta t$	$\Delta x_{min}/h$	Δt [ns]	Δx_{min} [nm]
(1)	918,000	9.25	43.09	0.50	29.4	29.4
(2)	468,000	5.04	19.21	0.50	51.1	50
(3)	130,200	16.26	57.02	0.50	15.9	50
(4)	972,000	9.94	21.49	0.20	13.6	40
(5)	285,696	65.47	98.86	0.11	1.40	33.3
(6)	275,280	9.98	21.39	0.37	2.88	37
(7)	198,400	32.09	45.30	0.32	0.039	32.2
(8)	359,040	40.54	45.49	0.16	0.0063	16

Table 6: The number of time steps per oscillation used in the numerical simulations. $P_v/\Delta t$ is the number of steps per oscillation in vacuum, $P_f/\Delta t$ is the number of steps per oscillation in fluid, Δt is the time step in vacumm, and Δx_{min} is the smallest side of a finite element in the three-dimensional model.

with different numbers of steps per oscillation $P_f/\Delta t$, see Fig. 16. The error in the quality factor as function of the time resolution is shown in Fig. 17. The expected time accuracy is first order. The fluid simulation with 35 time steps takes approximately 175 time steps to obtain the steady state solution. The fluid simulation takes approximately 3 days on a 3.2 GHz Xeon processor with 4GB of DDR memory. It is important to find a relationship between the quality factor and the time step. We found that increasing the time step made the quality factor more accurate. However, the computational cost was higher. The study shows that $20 \sim 40$ steps per oscillation is sufficient to resolve quality factor to within 5%.

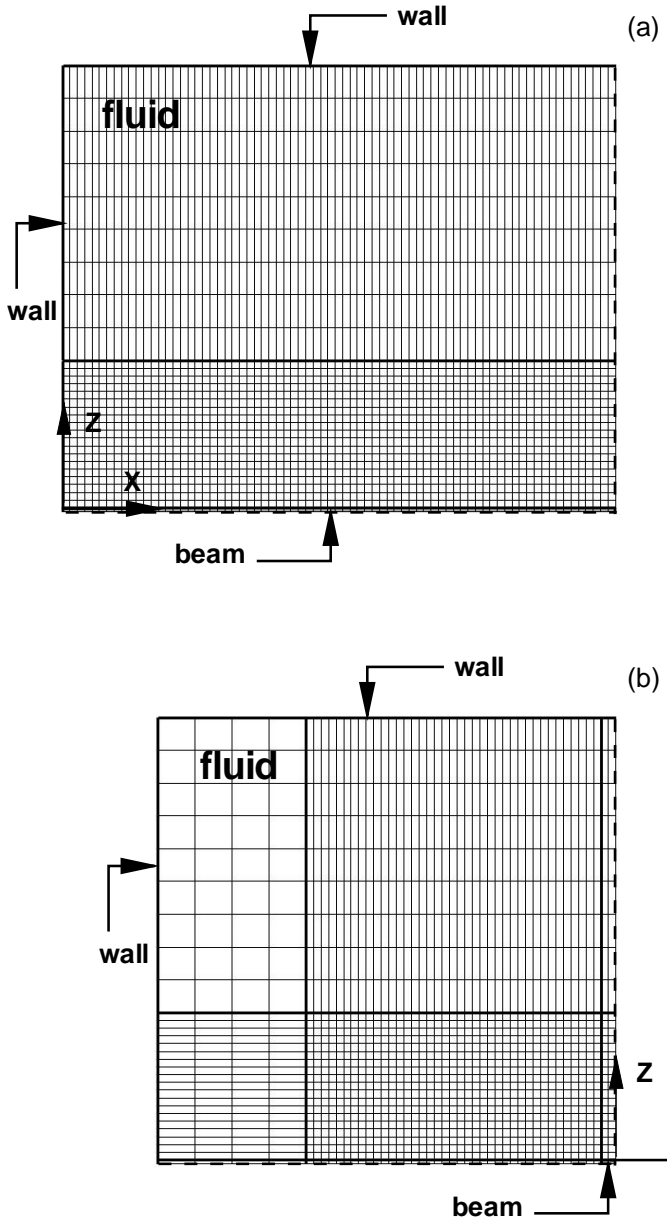


Figure 11: Grid resolution for cases (1-6). The schematic shows a single quadrant of the fluid and the beam domain. The doubly-clamped beam is located at the center of the volume. The volumes around the beam are composed of fluid. The external surfaces represent the walls bounding the fluid domain. The dashed lines are symmetry boundaries. (a) The $x - z$ plane grid resolution, symmetrically about x and z . (b) The $y - z$ plane grid resolution, symmetrically about y and z .

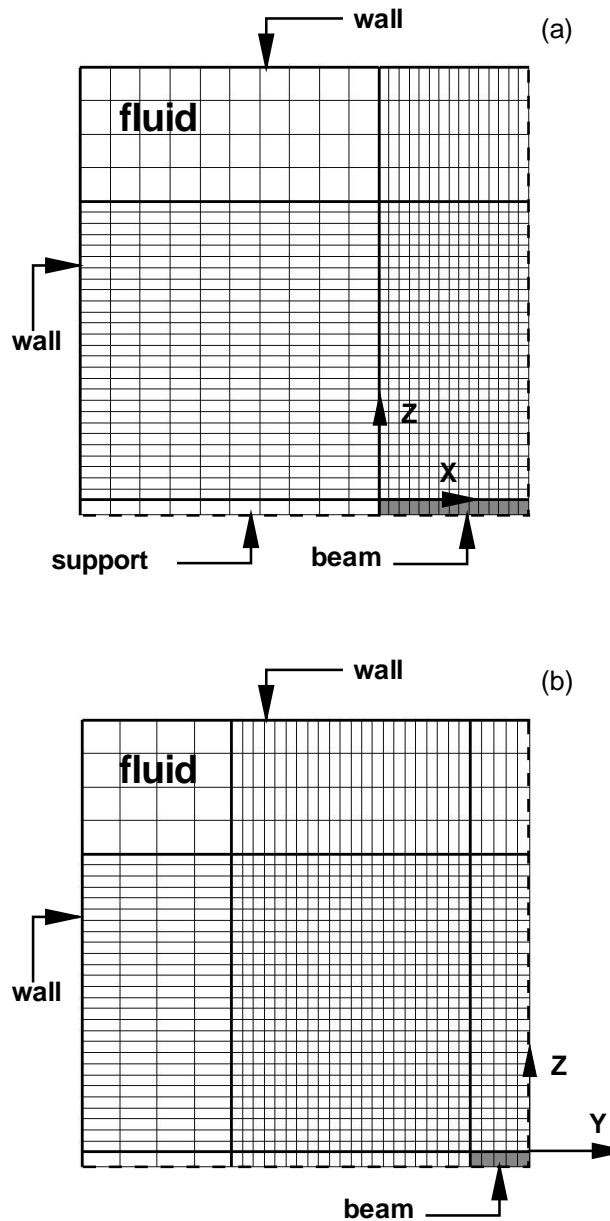


Figure 12: Grid resolution for cases (7-8). The schematic includes the fluid and beam. The schematic shows a single quadrant of the fluid and the beam domain. The doubly-clamped beam is located at the center of the volume fixed by two supports. The volumes around the beam are composed of fluid. The external surfaces represent the walls bounding the fluid domain. The dashed lines are symmetry boundaries. (a) The $x - z$ plane grid resolution, symmetrically about x and z . (b) The $y - z$ plane grid resolution, symmetrically about y and z .

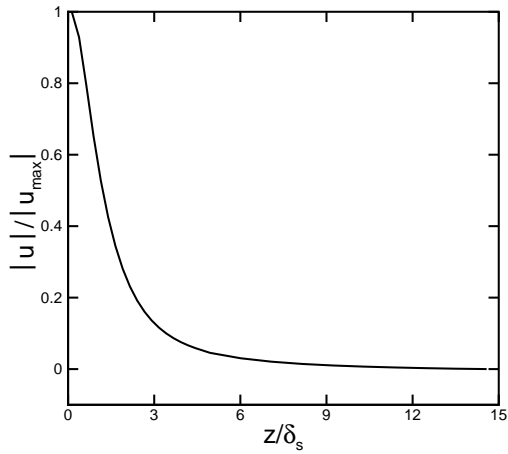


Figure 13: Normalized magnitude of the velocity between the beam and the wall in the z -direction. The velocity magnitude $|U|$ has been normalized by the maximum velocity $|U_{max}|$. The distance between the beam and the wall in the z -direction is normalized by the Stokes length δ_s .

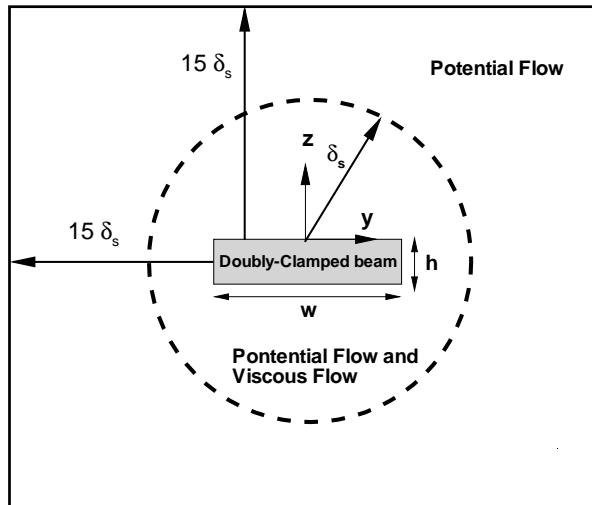


Figure 14: A schematic of the fluid flow regions around a doubly-clamped beam in the z - y plane. The figure is not drawn to scale. The outer box represents a no-slip wall. The beam surface is $15\delta_s$ from the wall.

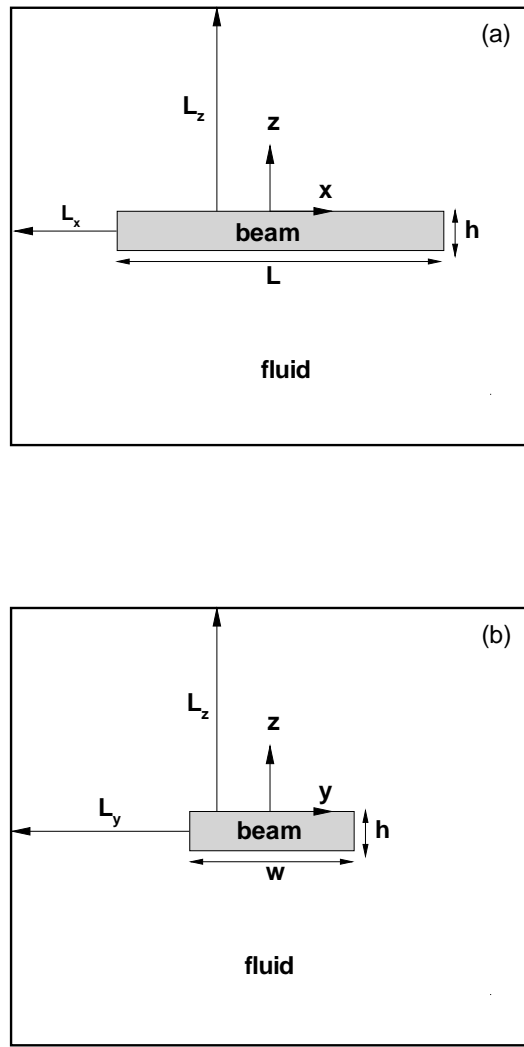


Figure 15: A schematic of the domain around a doubly-clamped beam of length L , width w , and height h with a uniform cross section. Shown are the wall-beam distance separations L_x , L_y , L_z in the x , y and z -directions respectively. (a) Numerical domain in the z - x plane. For cases 7 and 8, L_x represents the length of supports. (b) Numerical domain in the z - y plane.

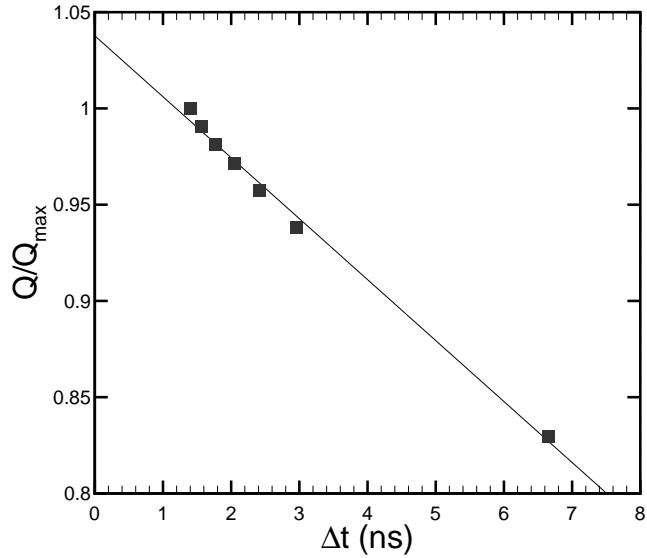


Figure 16: Quality factor as a function of the number of time steps. The geometry used is case (5) in Table 7. The solid line is a power fit to the data.

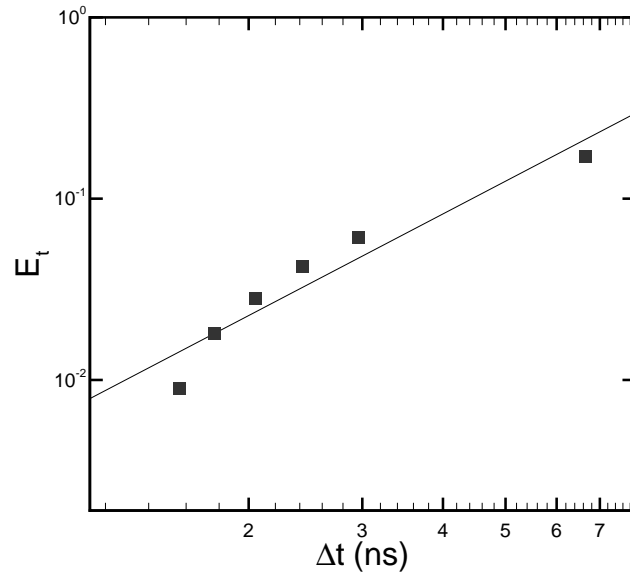


Figure 17: The error E_t as a function of time resolution. The geometry is case (5) in Table 7. The solid line is a power fit to the data and yields $E_t \sim \Delta t^{1.86}$.

5 Tailoring the Geometry of Doubly-Clamped Beam

5.1 Beam Geometry Study

As the baseline geometry we consider a doubly-clamped beam with length $L' = 15\mu\text{m}$, width $w' = 0.4\mu\text{m}$, and height $h' = 0.1\mu\text{m}$. This geometry is similar to what has been recently used in experiments demonstrating thermoelastic actuation in vacuum and air [7]. Here, we are interested in the beam dynamics in a viscous fluid and use water. This geometry is referred to as case (1) in Table 7 and we consider seven additional geometries which are chosen as systematic variations of the baseline geometry (L', w', h') . Also shown in Table 7 are the aspect ratios for the different geometries to give an idea of the range of geometries used and also to give some indication of the deviation from the ideal case of a long and thin beam used in analytical predictions [52].

Table 8 illustrates the deviations in geometry when compared with the baseline geometry of case 1. Also included are the beam properties that can be determined independent of the fluid dynamics which include the bulk spring constant k , the frequency parameter in vacuum R_0 , and the mass loading parameter T_0 . We have used finite element numerical simulations of the beams in vacuum to determine the numerical values of k and ω_0 for all of the geometries considered. Given this information one can use the analytical expressions to predict Q and ω_f which is illustrated in Fig. 5. From Table 8 it is clear that over four orders of magnitude of spring constant, over three orders of magnitude of frequency parameter, and over a single order of magnitude of the mass loading parameter are considered by the chosen variations in geometry.

We first quantify the stochastic dynamics of the baseline geometry. The numerical results for the autocorrelation of equilibrium fluctuations in beam displacement are shown in Fig. 18(a), and the noise spectrum is shown in Fig. 18(b). In each figure the baseline geometry is labeled w' . Extensive spatial and time

Case	L [μm]	w [μm]	h [μm]	L/w	L/h	w/h
(1)	15	0.4	0.1	37.5	150	4
(2)	15	0.8	0.1	18.75	150	8
(3)	15	1.2	0.1	12.5	150	12
(4)	15	0.4	0.2	37.5	75	2
(5)	15	0.4	0.3	37.5	50	1.33
(6)	5	0.4	0.1	12.5	50	4
(7)	1	0.4	0.1	2.5	10	4
(8)	0.4	0.4	0.1	1	4	4

Table 7: The eight geometries of doubly-clamped beams used in the numerical simulations. Case (1) is the baseline geometry and the remaining cases are variations of this geometry. The beam aspect ratios are L/w , L/h , and w/h . The horizontal lines separate the different studies performed: the baseline geometry, variation in width, variation in height, and variation in length. The beams are composed of silicon with Young's modulus $E = 210$ GPa, density $\rho_b = 3100$ kg/m³ and the fluid is water with $\rho_f = 997$ kg/m³, $\eta = 8.56 \times 10^{-4}$ kg/ms. All simulations are performed at room temperature with $T = 300\text{K}$.

resolution numerical tests have been performed to ensure the accuracy of our calculations. The autocorrelation curves are normalized using $k/k_B T$ where the value of k for each case is given in Table 8. The noise spectra have been normalized using the peak value $G(\omega_f)$. These figures illustrate that the dynamics of this micron scale beam in water are strongly damped. The value of the quality and resonant frequency in fluid using our numerical results are given in Table 9 and are $Q = 0.80$ and $\omega_f/\omega_0 = 0.22$. Also shown are the predictions from analytics using Eqs. (11) and (17) which yield $Q^\dagger = 0.68$ and $\omega_f/\omega_0^\dagger = 0.22$. The analytical predictions are quite accurate for the frequency drop while under predicting the quality factor for this geometry.

Next we consider the variation in the stochastic dynamics of the beam as a function of the beam width. In particular, we double and triple the beam width w while holding L and h constant. For increasing width the frequency parameter increases as $R_0 \sim w^2$ while the mass loading parameter increases as $T_0 \sim w$.

Case	L/L'	w/w'	h/h'	k [N/m]	R_0	T_0
(1)	1	1	1	0.40	1.08	1.01
(2)	1	2	1	0.83	4.55	2.02
(3)	1	3	1	1.21	10.19	3.03
(4)	1	1	2	3.19	2.17	0.51
(5)	1	1	3	10.82	3.19	0.34
(6)	1/3	1	1	10.92	10.20	1.01
(7)	1/15	1	1	1178.95	231.55	1.01
(8)	1/37.5	1	1	11413.04	1146.08	1.01

Table 8: The geometry variations with respect to the baseline geometry given by case (1) with (L', w', h') . Cases (2) and (3) explore increasing width, cases (4) and (5) explore increasing thickness, and cases (6)-(8) explore decreasing length. Also shown are the spring constant k , the frequency based Reynolds number in vacuum R_0 , and the mass loading parameter T_0 . The values of k and R_0 are determined using finite element simulations.

This has the effect of increasing the fluid inertia while simultaneously increasing the mass loading. These two counteracting effects suggest the increase in Q and ω_f will only be moderate. The autocorrelations and noise spectra from numerical simulations are shown in Fig. 18. The autocorrelation results exhibit both positively and negatively correlated results as expected with the dynamics becoming more underdamped as the width is increased. The noise spectra clearly illustrate that the peak value shifts to higher frequency and that the peak itself becomes sharper as the width increases. For case 1, the noise spectra has significant contributions at low frequency whereas for case 3 the noise spectra has become more symmetric with a Lorentzian shape.

Values for the quality and resonant frequency in fluid from our numerical results are given in Table 9. When compared to the quality for the baseline geometry Q' , the increase in quality is $Q/Q' = 1.29$ for doubling the width, and $Q/Q' = 1.71$ for tripling the width. The quality increases with increasing width however the magnitude of the quality is small indicating that the beam dynamics remain strongly damped. The increase in the value of ω_f/ω_0 is slightly

Case	R	ω_f/ω_0	Q	Q/Q'	$\omega_f/\omega_0^\dagger$	Q^\dagger
(1)	0.23	0.22	0.80	1.0	0.22	0.68
(2)	1.08	0.24	1.03	1.29	0.27	1.05
(3)	2.91	0.29	1.36	1.71	0.28	1.31
(4)	1.00	0.46	1.28	1.61	0.50	1.35
(5)	2.11	0.66	2.01	2.52	0.66	2.13
(6)	4.80	0.47	1.57	1.97	0.51	2.04
(7)	164.46	0.71	6.13	7.69	0.67	9.22
(8)	885.19	0.77	5.90	7.40	0.69	20.24

Table 9: The stochastic dynamics of the beams in fluid. Shown is the frequency based Reynolds number in fluid R , the reduction in the resonant frequency ω_f/ω_0 , and the quality factor Q . Also shown is the improvement of the quality with respect to that of case (1) given by $Q' = 0.8$. Q^\dagger and $\omega_f/\omega_0^\dagger$ are the results predicted from analytical theory using Eqs. (11) and (17).

less than what is found for Q . A comparison of our numerical values of ω_f and Q with the analytical predictions of Eqs. (11) and (17) are shown in Fig. 19. The circles are the results from our numerical simulations and the dashed line is the analytical prediction where $\xi = w/w'$ and w' is the width of the baseline geometry. It is clear that the analytical predictions remain quite accurate over this range. This includes case 3 where $L/w \approx w/h \approx 12$ and $L/h \gg 1$. Figure 19 indicates that magnitude of the increase in quality with increasing width is quite moderate. Furthermore, the increase in ω_f is quite small and becomes nearly flat at $\omega_f/\omega_0 \approx 0.24$ for $\xi \gtrsim 2$.

Next we consider the variation in beam dynamics as the height is increased. We consider the cases where h is doubled and tripled while the L and w are held constant. As the height is increased the frequency parameter increases as $R_0 \sim h$ whereas the mass loading parameter decreases as $T_0 \sim h^{-1}$. These two effects both contribute to increasing Q and ω_f . The normalized autocorrelations and noise spectra from our numerical simulations are shown in Fig. 20. The results clearly indicate an increasing value of both ω_f and Q and numerical values are

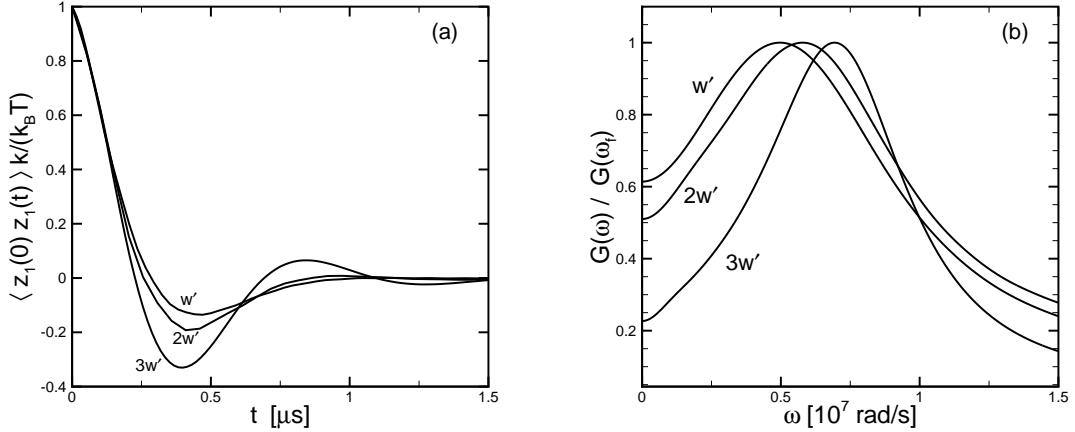


Figure 18: The autocorrelations and noise spectra of equilibrium fluctuations in beam displacement as a function of beam width from numerical results: case 1 (w'), case 2 ($2w'$), case 3 ($3w'$). (a) The autocorrelations, the results have been normalized using $k/(k_B T)$ for each case. (b) The noise spectra, the results have been normalized by the peak value for each case, $G(\omega_f)$.

given in Table 9. The relative increase in quality is $Q/Q' = 1.61$ when the height is doubled, and $Q/Q' = 2.52$ when the height is tripled. The increase in ω_f/ω_0 follows a similar trend.

A comparison of our numerical results with the predictions of theory is shown in Fig. 19 using $\xi = h/h'$. The square symbols are the numerical results and the solid line is the analytical prediction. It is clear that the increases in Q and ω_f are much larger for variations in height when compared to what was found for increases in beam width. The analytical predictions remain quite accurate and insightful over the range of aspect ratios explored by varying the beam height. We highlight that this includes case 5 where $w/h \approx 1$.

The last case we consider is decreasing the beam length while holding the width and height constant. In this case the frequency parameter increases rapidly as $R_0 \sim L^{-2}$ whereas T_0 remains constant. The autocorrelations and

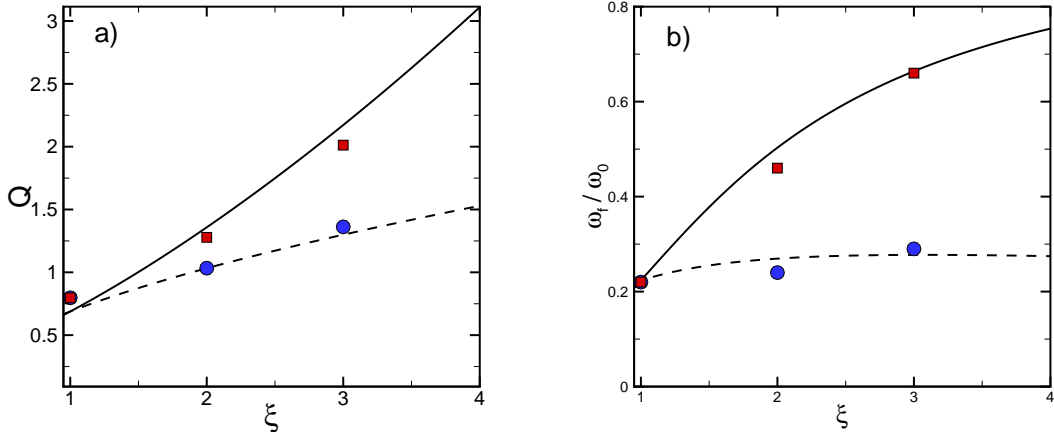


Figure 19: (color) Comparison of numerical results with analytical predictions for Q and ω_f as a function of width w and height h . The circles (blue) are for increasing width and the squares (red) are for increasing height. The solid line is the analytical prediction for increasing width and the dashed line is the analytical prediction for increasing height. To place all values on a single plot $\xi = w/w'$ for the varying width results and $\xi = h/h'$ for the varying height results.

noise spectra are shown in Fig. 21 which illustrate a significant increase in resonant frequency and quality. From Fig. 21(a) the results for the most extreme geometry explored, $L'/37.5$, clearly show the influence of higher harmonics. The numerical values of Q and ω_f from our numerical results are given Table 9. For case 8 where $L/L' = 37.5$ the increase in quality is $Q/Q' = 7.4$ and the reduction on the resonant frequency when compared to its value in vacuum is $\omega_f/\omega_0 = 0.77$ indicating significant changes are possible by changing the beam length.

The analytical predictions given in Table 9 show significant deviations from our numerical results. This is also illustrated in Fig. 21 where the triangles are the numerical results and the solid lines are the analytical predictions. For case 6 ($L/w = 12.5$) the analytical predictions are quite accurate. However, for case 7

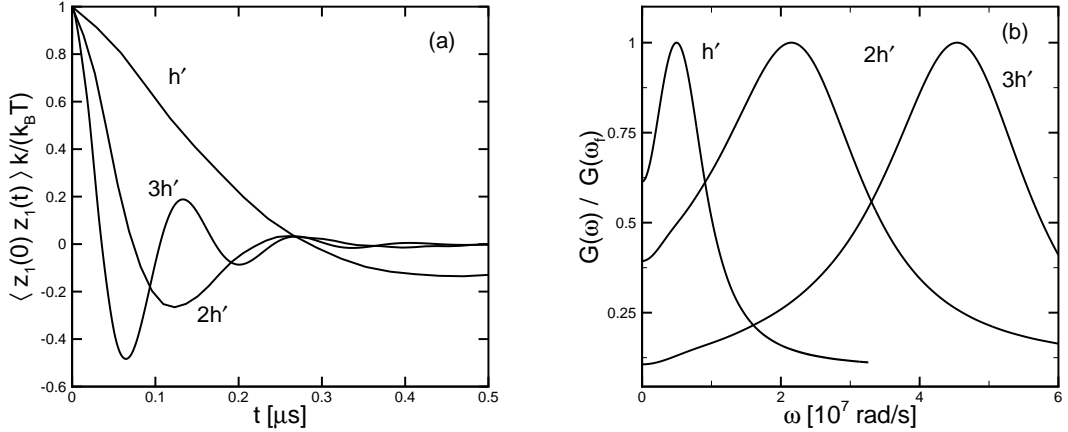


Figure 20: The autocorrelations and noise spectra as a function of beam height from numerical results: case 1 (h'), case 4 ($2h'$), case 5 ($3h'$). (a) The normalized autocorrelations. (b) The normalized noise spectra.

($L/w = 2.5$), and case 8 ($L/w = 1$) the analytical predictions over predict Q and under predict ω_f/ω_0 . The approximation of using the fluid flow from an infinite two-dimensional oscillating cylinder is no longer well justified. The numerical results suggest the presence of additional modes of fluid dissipation that are not captured in the two-dimensional theory.

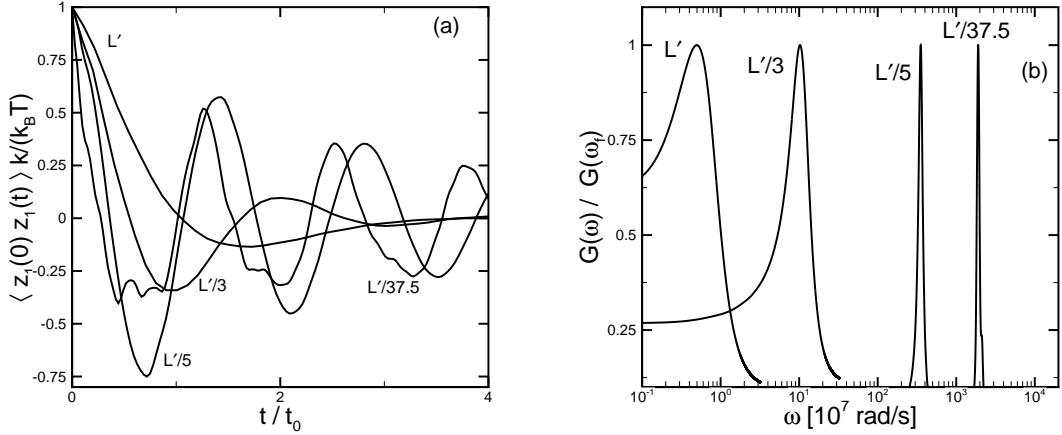


Figure 21: The autocorrelations and noise spectra as a function of beam length from numerical results: case 1 (L'), case 6 ($L'/3$), case 7 ($L'/5$), case 8 ($L'/37.5$). (a) The normalized autocorrelations. (b) The normalized noise spectra.

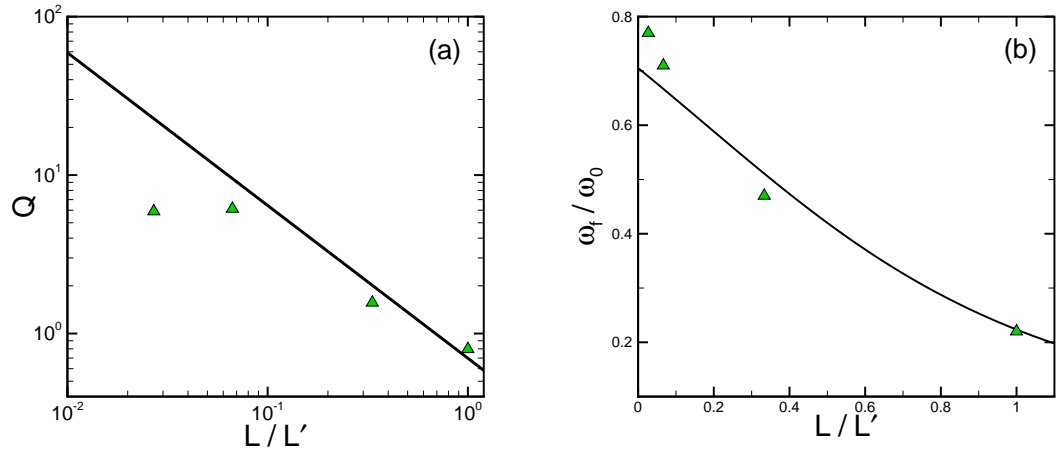


Figure 22: The variation of the quality Q , panel (a), and of the resonant frequency in fluid ω_f/ω_0 , panel (b), by decreasing the length L of the beam relative to the value of case (1) given by L' . The triangles are the results from numerical simulation and the solid line is the analytical prediction.

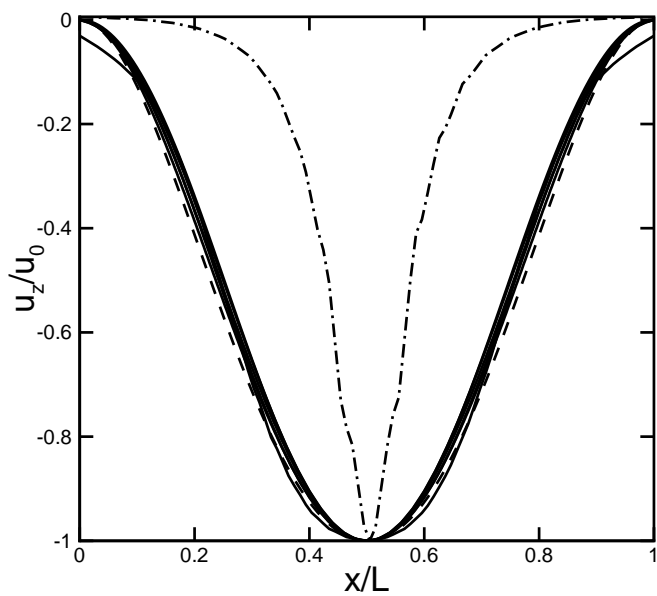


Figure 23: The transverse fluid velocity u_z for cases 1-8 along the line beginning at $(0.0, 0.0, 0.01\mu\text{m})$ and ending at $(L, 0.0, 0.01\mu\text{m})$ from the deterministic numerical simulations where the beam velocity is at its maximum value. The baseline geometry is shown as the dashed line, cases 2-7 are the solid lines, and case 8 is the dash-dot line.

6 Flow Field Analysis

6.1 Axial Flow Field

The flow field around the beam is three-dimensional. The characteristic two-dimensional flow field around the beam of case 1 and case 7 is shown respectively in Figs 24 and 25. These figures show the behavior of the flow field in the $x - y$ plane and $x - z$ plane. Figures 26 and 23 illustrate the magnitude of the fluid velocity in the transverse u_z and axial u_x directions, respectively. The velocities are plotted along a line beginning at $(0.0, 0.0, 0.01\mu\text{m})$ and ending at $(L, 0.0, 0.01\mu\text{m})$ for all cases. In our notation the fluid velocity in the (x, y, z) directions is (u_x, u_y, u_z) , see Fig. 6 for the definition of the coordinate directions (x, y, z) . The velocities are shown at the time when the velocity of the beam is at its maximum value which occurs when the center of the beam crosses $z = 0$ the first time during its ring down. The maximum value of u_z at this time is labeled u_0 and is used to normalize both the transverse and axial velocities. The axial direction is normalized by the beam length so that all cases can be represented on the same figure.

Figure 23 shows the transverse fluid velocity u_z for cases 1-8. The baseline geometry (dashed line) and cases 2-7 (solid lines) collapse onto a single curve with a shape similar to that of the fundamental mode of a doubly-clamped beam. Case 8 differs significantly with a much sharper peak indicating that its dynamics are quite different which is expected since this geometry is substantially different than the others.

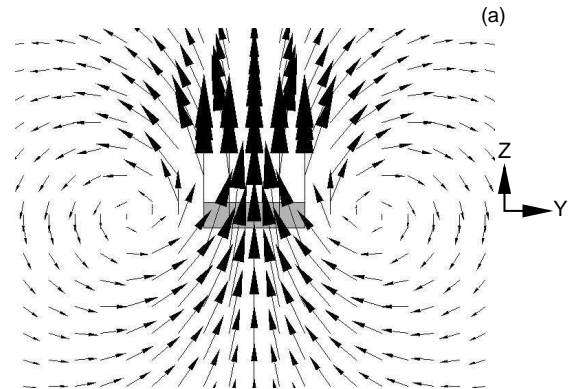
Figure 26(a) illustrates the normalized axial velocities u_x as the beam width and height are varied. In the approximation of a two-dimensional flow the axial velocity is identically zero and any deviations from this in the numerical results indicate fluid dynamics not considered in the analytical predictions. The bimodal shape of the curves is expected from the symmetry of the fundamental

mode. For $x > L/2$ the axial fluid velocity is positive and for $x < L/2$ it is negative. The baseline geometry is shown as the dashed line and has a negligible axial fluid velocity. At its maximum value it is only $\sim 2.5\%$ of the maximum transverse velocity u_0 . A similar trend is found for cases 2-5. As the width or height is increased the relative magnitude of the axial velocities increase. It is expected that if larger values of the width or height we computed the axial velocities would become significant and at this point the analytical predictions would show large deviations.

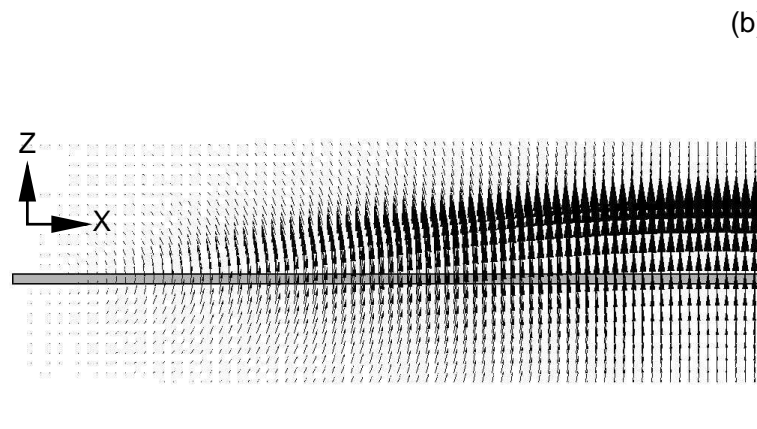
Figure 26(b) shows the relative value of the axial velocities as the length of the beam is decreased. The baseline geometry is included for reference as the dashed line. It is clear that the axial velocities are now quite significant and range from 10% to 40% of u_0 . The axial velocities do not vanish at $x = 0, L$ because the beams are held by rigid supports, see Fig. 6, and the lateral side walls of the numerical domain are distant. The axial velocities result in fluid dissipation not accounted for in the two-dimensional theory and contribute significantly to the lower values of Q found in the numerical simulations. Furthermore, ω_f from the numerical simulations are larger than the analytical predictions. The added mass in the simulations are smaller than the predicted values and this reduction is a direct result of the three dimensionality of the fluid flow. The maximum value of the relative axial velocity does not follow a monotonic trend with L because as the length becomes small the precise nature of the beam dynamics vary in a complicated manner. Overall, our results suggest that the relative magnitude of the axial velocity can be used to indicate the applicability of the two-dimensional theory.

In many microscale technologies the ability to sense small forces is important and therefore a small spring constant is desirable. In light of this, the improved performance, as measured by increased values of Q and ω_f with increasing w ,

increasing h or decreasing L all come at the price of reduced force sensitivity. Using Eq. (19) to estimate k yields its dependence upon geometry and the magnitude of the improved performance follows the same trend as increasing k . Overall, these tradeoffs would need to be balanced in a particular application.



(a)



(b)

Figure 24: Flow field velocity vectors around a doubly-clamped beam for case 1 at the instant of time where the beam is at its maximum velocity. (a) Flow field over the beam in the the $y - z$ plane. (b) Flow field around the beam in the $x - z$ plane. The dashed vertical line represents symmetry the boundary at $x = L/2$.

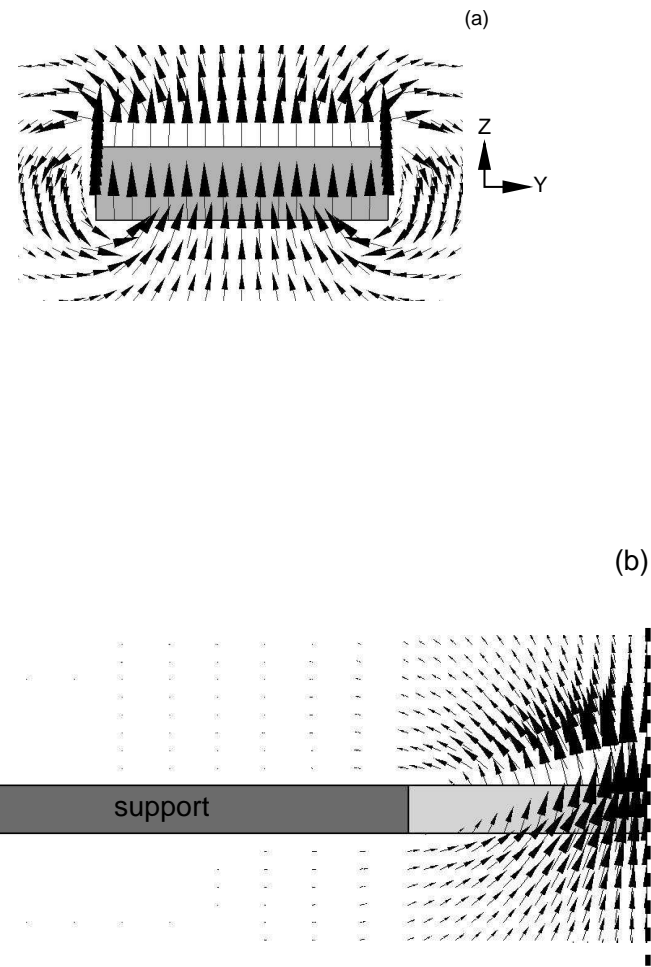


Figure 25: Flow field velocity vectors around the doubly-clamped beam for case 7 at the instant of time where the beam is at its maximum velocity. (a) Flow field over the beam in the the $y - z$ plane. (b) Flow field around the beam in the $x - z$ plane. The dashed vertical line represents the symmetry boundary at $x = L/2$.

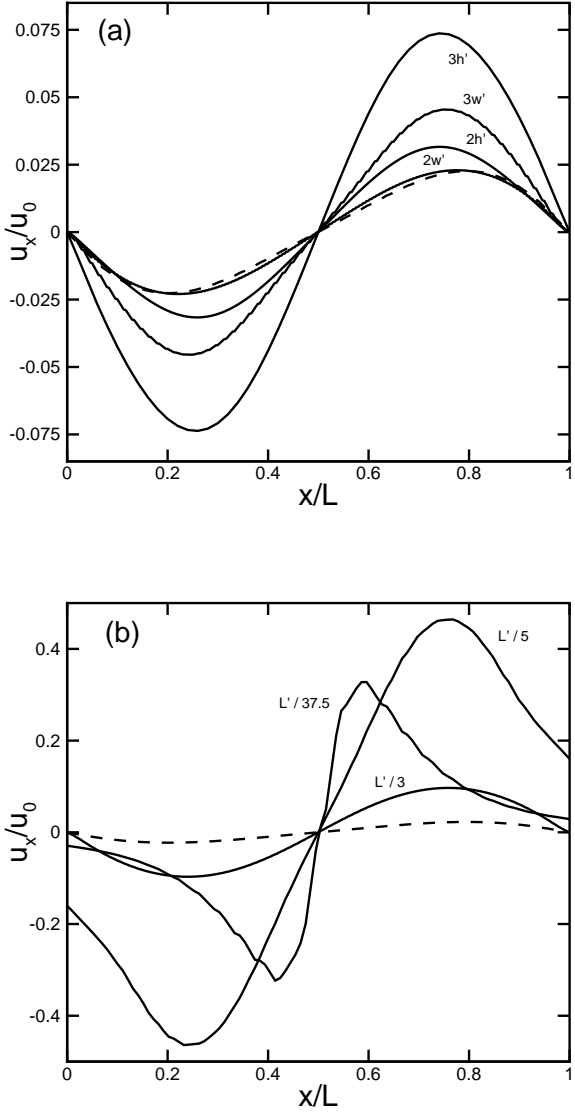


Figure 26: The normalized axial velocity from numerical simulation. (a) The axial velocity found varying the width and height of the baseline geometry. (b) The axial velocity found when decreasing the length of the baseline geometry. The results for the baseline geometry are given by the dashed line. The axial velocities are computed along a line in the x -direction with origin $(0,0,0.01\mu\text{m})$ and end-point $(L,0,0.01\mu\text{m})$, see Fig. 6 for definitions of coordinate directions. The velocity is normalized by u_0 for each case where u_0 is the maximum transverse velocity which occurs at $x = L/2$. The abscissa is normalized by the length L for each case.

7 Conclusions

The stochastic dynamics of micron and nanoscale elastic beams can be directly quantified using deterministic numerical computations for the precise geometries and conditions of experiment. To verify that the simulation parameters did not artificially affect the beam results, a series of validation studies were performed including a grid resolution study, a domain size study, a linear response study, and a time-step study. We have shown that the geometry of doubly-clamped beams can be tailored to overcome the strong fluid damping that occurs for small scale systems in a viscous fluid. Our numerical exploration has been used to build physical insights into the stochastic dynamics and to place realistic bounds upon the applicability of the two-dimensional theory. Overall, we find that the two dimensional theory is quite accurate far beyond what may have been expected based upon the underlying assumptions. When deviations do occur a significant factor are fluid velocities in the axial direction resulting in increased dissipation and a lower added mass. It is anticipated that these results will be useful in guiding the development of future experiments by providing the basis for predictions that cover a wide range of geometries. Furthermore, our results provide insight into the development of accurate theoretical models valid for the finite geometries used in experiment.

List of References

- [1] T. R. Albrecht and C. F. Quate. Atomic resolution imaging of a nonconductor by atomic force microscopy. *Journal of Applied Physics*, 62(7):2599–2602, 1987.
- [2] J. L. Arlett, J. R. Maloney, B. Gudlewski, M. Muluneh, and M. L. Roukes. Self-sensing micro- and nanocantilevers with attonewton-scale force resolution. *Nano Letters*, 6(5):1000–1006, 2006.
- [3] J. L. Arlett, M. R. Paul, J. E. Solomon, M. C. Cross, S. E. Raser, and M. L. Roukes. Bionems: Nanomechanical systems for single-molecule biophysics. *131st Nobel Symposium on Controlled Nanoscale Motion in Biological and Artificial Systems*, pages 241–270, 2005.
- [4] Y. Arntz, J. D. Seelig, H. P. Lang, J. Zhang, P. Hunziker, J. P. Ramseyer, E. Meyer, M. Hegner, and C. Gerber. Label-free protein assay based on a nanomechanical cantilever array. *Nanotechnology*, 14(1):86–90, 2003.
- [5] M. K. Baller, H. P. Lang, J. Fritz, C. Gerber, J. K. Gimzewski, U. Drechsler, H. Rothuizen, M. Despont, P. Vettiger, F. M. Battiston, J. P. Ramseyer, P. Fornaro, E. Meyer, and H. J. Guntherodt. A cantilever array-based artificial nose. *1st International Conference on Scanning Probe Microscopy, Cantilever Sensors and Nanostructures*, pages 1–9, 1999.
- [6] G. Bao and S. Suresh. Cell and molecular mechanics of biological materials. *Nature Materials*, 2(11):715–725, 2003.
- [7] I. Bargatin, I. Kozinsky, and M. L. Roukes. Efficient electrothermal actuation of multiple modes of high-frequency nanoelectromechanical resonators. *Applied Physics Letters*, 90(9), 2007.
- [8] S. Basak and A. Raman. Hydrodynamic loading of micrancantilevers vibrating in viscous fluids. *Journal of Applied Physics*, 99(114906), 2006.
- [9] G. Binning, C. F. Quate, and Ch. Gerber. Atomic force microscope. *Physical Review Letters*, 9(56):930–933, 1986.
- [10] T. Braun, V. Barwich, M. K. Ghatkesar, A. H. Bredekamp, C. Gerber, M. Hegner, and H. P. Lang. Micromechanical mass sensors for biomolecular detection in a physiological environment. *Physical Review E*, 72(3), 2005.

- [11] H. J. Butt and M. Jaschke. Calculation of thermal noise in atomic-force microscopy. *Nanotechnology*, 6(1):1–7, 1995.
- [12] C. Carvajal. The fluid-coupled motion of micro and nanoscale cantilevers. *Master's Thesis*, Virginia Tech, 2007.
- [13] M. Clark. The stochastic dynamics of an array of atomic force microscopes in viscous fluid. *PhD Thesis*, Virginia Tech, 2008.
- [14] M. T. Clark and M. R. Paul. The stochastic dynamics of an array of atomic force microscopes in a viscous fluid. *International Journal of Non-Linear Mechanics*, 42(4):690–696, 2007.
- [15] R. J. Clarke, S. M. Cox, P. M. Williams, and O. E. Jensen. The drag on a microcantilever oscillating near a wall. *Journal of Fluid Mechanics*, 545:397–426, 2005.
- [16] R. J. Clarke, O. E. Jensen, J. Billingham, A. P. Pearson, and P. M. Williams. Stochastic elastohydrodynamics of a microcantilever oscillating near a wall. *Physical Review Letters*, 96(5), 2006.
- [17] R. J. Clarke, O. E. Jensen, J. Billingham, and P. M. Williams. Three-dimensional flow due to a microcantilever oscillating near a wall: an unsteady slender-body analysis. *Proceedings of the Royal Society A: Mathematical Physical and Engineering Sciences*, 462(2067):913–933, 2006.
- [18] H. Clausen-Schaumann, R. Seitz, and M. Krautbauer. Force spectroscopy with single bio-molecules. *Current Opinion in Chemical Biology*, 4(5):524530, 2000.
- [19] A. N. Cleland and M. L. Roukes. Fabrication of high frequency nanometer scale mechanical resonators from bulk Si crystals. *Applied Physics Letters*, 69(18):2653–2655, 1996.
- [20] A. N. Cleland and M. L. Roukes. External control of dissipation in a nanometer-scale radiofrequency mechanical resonator. *Sensors and Actuators A: Physical*, 72(3):256–261, 1999.
- [21] Private communication with Michael Roukes. Caltech 114-36, Pasadena CA 91125.

- [22] Z. G. Djuric and I. M. Jokic. Thermomechanical noise of nanooscillators with time-dependent mass. *32nd International Conference on Micro- and Nano-Engineering*, 84:1639–1642, 2007.
- [23] K. L. Ekinci and M. L. Roukes. Nanoelectromechanical systems. *Review of Scientific Instruments*, 76(6), 2005.
- [24] R. Garcia and R. Perez. Dynamic atomic force microscopy methods. *Surface Science Reports*, 47(6-8):197–301, 2002.
- [25] M. K. Ghatkesar, T. Braun, V. Barwick, J. P. Ramseyer, C. Gerber, M. Hegner, and H. P. Lang. Resonating modes of vibrating microcantilevers in liquid. *Applied Physics Letters*, 92(4), 2008.
- [26] M. Godin, A. K. Bryan, T. P. Burg, K. Babcock, and S. R. Manalis. Measuring the mass, density, and size of particles and cells using a suspended microchannel resonator. *Applied Physics Letters*, 91(12), 2007.
- [27] C. P. Green and J. E. Sader. Frequency response of cantilever beams immersed in viscous fluids near a solid surface with applications to the atomic force microscope. *Journal of Applied Physics*, 98(11), 2005.
- [28] ESI CFD Headquarters. Huntsville AL 25806. We use the CFD-ACE+ solver.
- [29] J. H. Hoh, J. P. Cleveland, C. B. Prater, J. P. Revel, and P. K. Hansma. Quantized adhesion detected with the atomic force microscope. *Journal of the American Chemical Society*, 114(12):4917–4918, 1992.
- [30] A. Karniadakis, G. Beskok and N. Aluru. Microflows and nanoflows fundamentals and simulation. *Springer*, 2001.
- [31] L. Khine, M. Palaniapan, L. C. Shao, and W. K. Wong. Characterization of SOI Lamé-mode square resonators. *IEEE International Frequency Control Symposium*, pages 625–628, 2008.
- [32] L. D. Landau and E. M. Lifshitz. Theory of elasticity. *Butterworth-Heinemann*, 1959.
- [33] J. Ma, H. Jimenez and R. Rajagopalan. Brownian fluctuation spectroscopy using atomic force microscopes. *Langmuir*, 16(114906):2254–2261, 2000.

- [34] S. C. Masmanidis, R. B. Karabalin, I. De Vlaminck, G. Borghs, M. R. Freeman, and M. L. Roukes. Multifunctional nanomechanical systems via tunably coupled piezoelectric actuation. *Science*, 317(5839):780–783, 2007.
- [35] R. L. Panton. Incompressible flow. *John Wiley and Sons, Inc*, 2005.
- [36] M. R. Paul, M. T. Clark, and M. C. Cross. The stochastic dynamics of micron and nanoscale elastic cantilevers in fluid: fluctuations from dissipation. *Nanotechnology*, 17(17):4502–4513, 2006.
- [37] M. R. Paul and M. C. Cross. Stochastic dynamics of nanoscale mechanical oscillators immersed in a viscous fluid. *Physical Review Letters*, 92(23), 2004.
- [38] J. Raman, A. Melcher and R. Tung. Cantilever dynamics in atomic force microscopy. *Nano Today*, 3(1-2):20–27, 2008.
- [39] L. Rosenhead. Laminar boundary layers. *Oxford University Press*, 1963.
- [40] M. L. Roukes. Nanoelectromechanical systems. *Technical Digest of the 2000 Solid-State Sensor and Actuator Workshop, Cleveland: Transducer Research Foundation*, 2000.
- [41] J. E. Sader. Frequency response of cantilever beams immersed in viscous fluids with applications to the atomic force microscope. *Journal of Applied Physics*, 84(1):64–76, 1998.
- [42] L. Sekaric, M. Zalalutdinov, R. B. Bhiladvala, A. T. Zehnder, J. M. Parpia, and H. G. Craighead. Operation of nanomechanical resonant structures in air. *Applied Physics Letters*, 81(14):2641–2643, 2002.
- [43] L. C. Shao, M. Palaniapan, L. Khine, and W. W. Tan. Nonlinear behavior of Lamé-mode SOI bulk resonator. *IEEE International Frequency Control Symposium*, pages 646–650, 2008.
- [44] S. Son, W. H. Grover, T. P. Burg, and S. R. Manalis. Suspended microchannel resonators for ultralow volume universal detection. *Analytical Chemistry*, 80(12):4757–4760, 2008.
- [45] R. W. Stark, T. Drobek, and W. M. Heckl. Thermomechanical noise of a free V-shaped cantilever for atomic-force microscopy. *2nd International Conference on Scanning Probe Microscopy, Sensors, and Nanostructures*, pages 207–215, 2000.

- [46] G. G. Stokes. Laminar boundary layers. *Trans. Cambridge Philos. Soc.*, 9:8, 1951.
- [47] J. Tamayo, A. D. L. Humphris, R. J. Owen, and M. J. Miles. High-Q dynamic force microscopy in liquid and its application to living cells. *Bioophysical Journal*, 81(1):526–537, 2001.
- [48] E. O. Tuck. *J. Eng. Math*, 3:29, 1969.
- [49] C. A. Van Eysden and J. E. Sader. Small amplitude oscillations of a flexible thin blade in a viscous fluid: Exact analytical solution. *Physics of Fluids*, 18(12), 2006.
- [50] C. A. Van Eysden and J. E. Sader. Frequency response of cantilever beams immersed in viscous fluids with applications to the atomic force microscope: Arbitrary mode order. *Journal of Applied Physics*, 101(4), 2007.
- [51] S. S. Verbridge, L. M. Bellan, J. M. Parpia, and H. G. Craighead. Optically driven resonance of nanoscale flexural oscillators in liquid. *Nano Letters*, 6(9):2109–2114, 2006.
- [52] M. Villa and M. R. Paul. The stochastic dynamics of micron scale doubly-clamped beams in a viscous fluid. *Unpublished*.
- [53] G. M. Whitesides. The ‘right’ size in nanobiotechnology. *Nature Biotechnology*, 21(10):1161–1165, 2003.
- [54] X. Xu and A. Raman. Comparative dynamics of magnetically, acoustically, and Brownian motion driven microcantilevers in liquids. *Journal of Applied Physics*, 102(034303), 2007.
- [55] H. Q. Yang and V. B. Makhijani. A strongly-coupled pressure-based CFD algorithm for fluid-structure interaction. *American Institute of Aeronautics and Astronautics*, 94(0179):110, 1994.
- [56] Y. T. Yang, C. Callegari, X. L. Feng, K. L. Ekinci, and M. L. Roukes. Zeptogram-scale nanomechanical mass sensing. *Nano Letters*, 6(4):583–586, 2006.
- [57] C. Zandonella. The tiny toolkit. *Nature*, 423(6938):374–374, 2003.